Politecnico
di Bari

Department of Mechanics, Mathematics and Management
MECHANICAL AND MANAGEMENT ENGINEERING
Ph.D. Program
SSD: ING-IND/14–Mechanical Design and Machine Construction

Final Dissertation

STICK-SLIP TRANSITION AND DYNAMIC CYCLIC RESPONSE OF FRICTION DAMPED SYSTEMS

by

Antonio Papangelo
_____

Referees:

Prof. A. STROZZI

Prof. N. HOFFMANN

Supervisors:

Prof. Ing. Michele CIAVARELLA

_____

Prof. Ing. Luciano AFFERRANTE

_____

Coordinator of Ph.D Program:

Prof. Ing. G.P. Demelio

_____
_____

XXIX cycle, 2014-2016

"Per aspera sic itur ad astra."

Seneca, Hercules furens, atto II v. 437

To Elena,

for having been always by my side,

since the first day of these 3 years…

Contents

Outline

This thesis is subdivided into two parts: in the first we analyze the transition from static to dynamic friction with some emphasis on the implication of using more refined friction laws (with respect to the simple Coulomb model) while in the second part we study the cyclic response of dynamical systems that experience friction. Particularly, in the first part we will take inspiration from some recent experiments from the group of Prof. Fineberg to tackle some partial slip contact problems, with the idea in mind of providing analytical models that can, in some extent, interpreter some of the numerous experimental evidences that came from the direct observation of the sliding phenomena. In the chapters 1-2 a brief introduction of the equations that govern the contact of elastic bodies and the experimental test rig used in the experiments is presented. In chapter 3 the partial slip problem of a flat square-ended punch pressed against an half-plane and tangentially loaded above the contact interface is studied, then a FEM of the Prof. Fineberg experimental test rig will be proposed to avoid the hypothesis of half-plane elasticity, with good agreement between numerical and experimental results. In chapter 4 the implications of using a slip weakening friction law instead of the classical Coulomb law are discussed and an energetic criterion for slip inception is derived, which we will call "Griffith friction model". In chapter 5, using this "Griffith friction", the partial slip problem for different plane geometries (power law punches and sinusoidal profile) is solved.

In the second part of the thesis we will focus our attention on the dynamic response of mechanical systems subjected to friction. In chapter 7 a very simple model of structure subjected to dry friction is studied, constituted by a single degree of freedom system subjected to a periodical tangential excitation and a (possibly) varying normal load. First we compare the quasi-static solution with the dynamic solution in the limit of very low excitation frequency, then we study (in the bounded regime) how the peak displacement and dissipation is related to the phase shift between the normal and the tangential load. In chapter 8 the dynamical behavior of a mass-spring-viscous damper structure linked to a massless Coulomb damper is studied with attention to the regime that minimize the vibration amplitude of the mass. Finally in chapter 9, we study a friction-excited nonlinear oscillator chain, where a polynomial nonlinearity is introduced in the system. We focus our attention on the multiplicity of solutions that are proven to exist in certain parameter ranges which leads to a bifurcation pattern similar to the snaking bifurcations. In the end conclusions and possible developments of the present work are proposed.

Part II

Part II: Cyclic response of friction damped mechanical systems

Chapter 6

Dampers and joints in mechanical systems

Dynamic frictional problems have received considerable interest in science and technology for the evident relevance in many fields of application. The most engineering structures from automotive, aerospace and civil engineering are assembled by joints such as bolted, riveted and clamped joints. Many of them require specific devices (dampers) to damp vibrations of a structure/component and decrease peak stresses and wear, increasing life fatigue. Frictional devices make use of many physical concepts: viscosity and viscoelasticity ([71],[73],[74]), shape memory alloys field [72], hysteresis, inertia (like in tuned mass dampers) ([75],[76]), and finally dry friction ([74],[77],[78]). The latter is very commonly used as it is almost always available and low cost devices can be designed by industry. In many situations damping is ensured by the presence of joints such as bolted, riveted and clamped joints, that are not designed as a dampers, but can be one of the main sources of energy dissipation in metal structures ([79],[80],[81]). This is due to the microslip events that take place at the contact interfaces. One of the biggest challenges for the future mechanical designers will be to effectively design joints in order to obtain the desired stiffness and damping behavior. Nowadays, joints are considered a liability and not a resource of the design process as predictive models are practically not available. One attempt has been done with the Iwan model [82] for joints, but a lot needs to be done. In fact, we have seen in the first part of this thesis that dry friction governing laws are highly nonlinear due to the "sign" function corresponding to the step change of frictional force magnitude with the change of slip direction. In this part of the thesis we will analyze the dynamic response of some mechanical models, with the aim to gather insights on what we should expect when analyzing more complicated assembled structure. We will concentrate our studies on the peak vibration amplitude and energy dissipation of some lumped mechanical systems, starting from a single degree of freedom oscillator and ending with a chain of nonlinear oscillators with 12 degrees of freedom. In the latter case we will show that, for a given range of parameters, friction nonlinearities can lead to a multiplicity of stable/unstable solutions.

Chapter 7

Coulomb frictional oscillator

In this chapter, we study first a simple Coulomb frictional oscillator with harmonic tangential load, but with constant normal load. It is found that the quasi-static solution, obtaining by cancelling inertia terms in the equilibrium equations, does not coincide with the limit of the full dynamic solution at low frequencies. It captures approximately the displacement peak, but the velocity peak is not correctly estimated, due to the stick-slip phenomenon. In the second part we let the normal load to be harmonic. Some additional closed form results are given for this problem for both the quasi-static limit and the full dynamic regime. We find in particular the regime where normal load is high enough to obtain a bounded displacement at all frequencies, which is of particular interest for "optimal" damping. Contrary to the quasi-static prediction, the effect of normal load variation can decrease the peak displacement amplitude for in phase loading up to the 80% while, similar to the quasi-static prediction, it can lead to a very large increase for quadrature loading. Similar pattern is found for the frictional dissipation per cycle.

7.1 Introduction

For viscous damping the resisting force is proportional to the relative speed, and hence becomes increasingly and monotonically negligible when frequency is reduced, so that the quasi-static limit is a good approximation to a full dynamic analysis for many problems of engineering interest, as it is apparent from the widespread use of quasi-static analysis. Vice versa, in dry friction, the resisting force has no dependence on the velocity (at least, as a first approximation as in Coulomb law), and only depends on slip direction. This has strong implications for the quasi-static limit, as it will be made clearer in the following paragraphs in a very simple system subject to harmonic loading.

Notice that "quasi-static" is a quite confusing term in the literature, since it may have perhaps three different meanings (see Figure 7.1):

1. in the mechanics of continua, the approximation neglecting wave motion, where the inertia forces as rigid bodies may be retained, but reducing the bodies to discrete spring-mass models see eg. ([83]) — we would rather call it a "discrete" model of a continuum.

2. still in mechanics of continua, the "quasi-static" approximation may be intended as the solution where inertia terms are eliminated from the outset, but the bodies remain continua. In the context of contact mechanics, this is the case for many classical solutions, from the Hertz problem, to the Cattaneo-Mindlin one, and so on (see the text of Johnson [2]).

3. finally, as in the present paper, "quasi-static" approximation of a discrete, like spring-mass model, may be that obtained by removing the mass term from the solution.
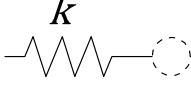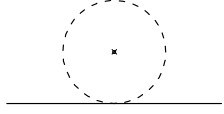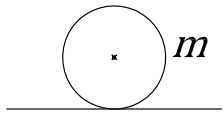
	DISCRETE	*CONTINUUM*
m=0	QuaSi-sTatiC *k*	Classical Hertz, Cattaneo-Mindlin etc...
m>0	Spring-Mass Model *k* *m*	Mesh Dependent *m*

Fig. 7.1 Possible meaning of quasi-static approximation, and our case (QSTC).

At the other extreme, the true "dynamic" of a frictional system, with wave motion, and using Coulomb law not only requires a very rich and demanding simulation for a mechanical system [84], but may involve results that are mesh-dependent. In fact, uniform sliding is unstable for a very wide range of friction coefficient and ratios of elastic constants ([85],[86],[87]). Thus pressure waves of large wavenumber grow with an increasingly large exponential rate, numerical convergence with grid refinement may not be achieved [88], unless more sophisticated friction laws are used for regularization ([88],[89]).

Numerical solutions to cyclic frictional problems typically imply a costly time-marching solution, or else specific algorithms which assume a certain form of the periodic response, like in the harmonic balance technique. Analytical solutions, even for simple frictional dynamic systems, are generally approximate, assuming treatable functional form for the displacement and velocity evolution. Even for the single DOF oscillator, which we will consider in the present paper, considerable effort is required for analytical results ([90],[91]). This makes them valid only for high enough frequencies when there are zero stops in the steady state trajectory. Towards the quasi-static limit, the number of stops in the dynamic solution increases, and hence, as we shall see, the quasi-static "limit" solution is not unambiguously defined. The solution we shall call QSTC (Quasi-STatiC) is the one obtained by neglecting altogether the inertia term in the equation of motion, but since this gives only 2 stops per cycle, it does not correspond strictly speaking to any of the dynamic solutions, not even in the limit. In fact, we shall find that the limit velocity is not correctly predicted by the QSTC solution.

The idea of examining more carefully the quasi-static limit came to the authors in particular reading the interesting recent paper of Brake and Hills [92] who have suggested, at least for the geometry they considered (two coaxial cylinders under constant normal load and torsional oscillations), an interesting 10% rule, which we could summarize as follows: *for excitation frequencies that are 10% of the fundamental resonance of a system, there is a 10% difference between the dynamic solution and quasi-static solution, at least as regarding the inception of slip.* Their analysis is considerably different and has more to do with the approximation of a continuum to a discrete

model of a rather special type (a spring-mass model where stiffness is eliminated as there are no constraints), rather than our eliminating the mass in a discrete model. However, it is their general attempt to define rules for the difference between quasi-static and dynamic solutions in frictional problems that we shall try to follow as example.

Therefore, we considered the simplest frictional system of all, a spring-mass model with just 1 degree of freedom (since the vertical DOF has no dynamics), but we looked more generally than it has been done so far in the literature, at the difference between the full dynamic solution (DYN) and the QSTC one (where we eliminate the mass), comparing the two for frequency of loading decreasing to zero. The results for the QSTC limit can be obtained trivially, whereas the correct DYN solution require careful numerical investigation, as done here using two possible algorithms: a standard time-marching Newmark scheme, or a piecewise analytical solution. The results show that we should reconsider what we mean by "quasi-static" limit in frictional system, since it may well not be in all respects the solution of the problem when mass is removed. In this sense, looking for a general rule to replace the full dynamic solution with a QSTC solution may actually be meaningless, as it may divert attention from the dynamic problems like stick-slip which may occur (and actually do occur in particular) at low frequency of loading. The QSTC limit turns out to be close to the dynamic one only in the presence of very large additional viscous damping in the structure (close to critical).

7.2 The model

Consider a rigid horizontal support on which a concentrated mass slides (Fig. 7.2). The mass is linked to a fixed wall by means of a spring of stiffness k and the friction between the horizontal plane and the mass is assumed to be Coulomb-like with a friction coefficient equal to f (no difference between static and dynamic value).
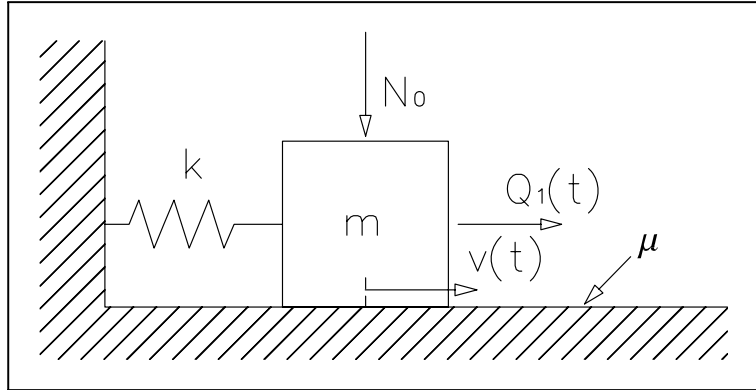
Fig. 7.2 The spring-mass model oscillator damped by Coulomb friction, under constant normal load and harmonic tangential load.

We consider a constant normal and tangential load of the form

$$N(t) = N_0 \tag{7.1}$$

$$Q(t) = Q_1 \sin(\omega_d t) \tag{7.2}$$

where $N_0 > 0$, $Q_1 > 0$ is the amplitude of tangential load and ω_d is the angular frequency of the loading. This case corresponds to that considered by Hong and Liu in ([93],[91]).

7.3   Quasi-static solution

Let us first consider the quasi-static limit (no inertia) for the system in Figure 7.2; if the mass is moving towards the positive direction due to equilibrium we can write the displacement as

$$v(t) = \frac{Q_1}{k} \sin(\omega_d t) - \frac{fN_0}{k} \tag{7.3}$$

The maximum positive displacement will be reached when $\sin(\omega_d t)$ will reach its maximum value 1, so

$$v_{\max}^+ = \frac{Q_1}{k} - \frac{fN_0}{k} = \frac{Q_1}{k}(1 - \beta) > 0 \tag{7.4}$$

where β is a dimensionless parameter

$$0 < \beta = \frac{fN_0}{Q_1} < 1 \tag{7.5}$$

The condition $\beta < 1$ is needed to avoid full stick for constant normal load. If the mass is moving towards the negative direction the equation of motion leads to:

$$v(t) = \frac{Q_1}{k} \sin(\omega_d t) + \frac{fN_0}{k} \tag{7.6}$$

The maximum negative displacement will be reached when $\sin(\omega_d t)$ will reach its minimum value -1, so

$$v_{\max}^- = -\frac{Q_1}{k} + \frac{fN_0}{k} = -\frac{Q_1}{k}(1 - \beta) < 0 \tag{7.7}$$

Of course the (7.4) and (7.7) are equal in modulus as the loading is symmetric, so the absolute maximum displacement is

$$v_{qstc}|_{\max} = \frac{Q_1}{k}(1 - \beta) \tag{7.8}$$

Equating equation (7.4) with equation (7.6) the onset of backward slip t_{bs}, is obtained

$$g_1 = \sin(\omega_d t_{bs}) = 1 - 2\beta \tag{7.9}$$

Following the same reasoning for the onset of forward slip, we equate (7.7) and (7.3), to obtain

$$g_2 = \sin(\omega_d t_{fs}) = -1 + 2\beta \tag{7.10}$$

As $-1 \leqslant \sin(\omega_d t) \leqslant 1$ we have solutions only for $0 \leqslant \beta \leqslant 1$. Notice that the equations (7.9) and (7.10) are the simplified version of those found by Jang and Barber in [94] for the case of varying normal load.

Differentiating with respect to the time (7.6) and (7.3) the velocity is obtained, for both the cases of backward and forward slip

$$\dot{v}(t) = \omega_d \frac{Q_1}{k} \cos(\omega_d t) \tag{7.11}$$

If backward slip commences when $g_1 \geqslant 0$, then $\cos(\omega_d t)$ hasn't already reached its minimum value, so the maximum negative velocity in magnitude will be $|\dot{v}(t)| = \omega_d \frac{Q_1}{k}$ whereas if $g_1 < 0$ the maximum negative velocity in magnitude will be exactly that reached in the time instant for which the backward slip starts which yields to $\cos(\omega_d t_{bs}) = \sqrt{1 - g_1^2}$. For the case of forward slip we need a similar reasoning, that leads to the following general rule:

$$|\dot{v}_{qstc}|_{\max} = \begin{cases} \omega_d \frac{Q_1}{k} & \text{for } 0 \leqslant \beta \leqslant \frac{1}{2} \\ 2\frac{Q_1}{k}\omega_d\sqrt{\beta(1-\beta)} & \text{for } \frac{1}{2} \leqslant \beta \leqslant 1 \end{cases} \tag{7.12}$$

Due to the symmetry of the load, the dissipated energy per cycle within the quasi-static limit can be calculated for half cycle (for example for the backward slip) which leads to

$$W_{qstc} = -2\int_{t_{bs}}^{t_{stop}} F\dot{v}dt = -2\int_{g_1}^{-1} fN_0\frac{Q_1}{k}dg \rightarrow$$

$$W_{qstc} = 4\frac{Q_1^2}{k}\beta(1-\beta) \tag{7.13}$$

where we define $g(t) = \sin(\omega_d t)$, and use equation (7.9).

7.4 The dynamic solution

7.4.1 Piecewise analytical solution

Consider that the system sketched in Figure 7.2 is in a phase of slip; from the linear momentum balance in the horizontal direction

$$m\ddot{v}(t) + kv(t) = Q_1\sin(\omega_d t) - sign(\dot{v})fN_0 \tag{7.14}$$

where $v(t)$ is the position of the mass at the time t. To obtain the temporal evolution of the system, we subdivide our temporal window in intervals in which the mass is in stick or in slip. For the first case the solution of the problem is trivial, while for the slip phase Hong and Liu found the solution of (7.14) in [93] that rearranged is also reported hereafter:

$$v(t) = v(t_i) - \left[v(t_i) + sign(\dot{v})\frac{fN_0}{k}\right]\{1 - \cos[\omega_n(t - t_i)]\} +$$

$$+ \frac{\dot{v}(t_i)}{\omega_n}\sin[\omega_n(t - t_i)] +$$

$$+ \frac{Q_1}{k(1 - \Omega^2)}\{\sin(\omega_d t) - \sin(\omega_d t_i)\cos[\omega_n(t - t_i)] +$$

$$-\Omega\cos(\omega_d t_i)\sin[\omega_n(t - t_i)]\} \tag{7.15}$$

where $v(t_i)$ and $\dot{v}(t_i)$ are the initial conditions.

Notice that the mass in a forward slip phase could turn both to a backward slip phase and to a stick phase. In each of those cases, there will be a time instant in which the velocity vanishes. To simplify the solution of the problem, we look for a piecewise analytical solution for which, in each interval considered, the velocity retains the same sign. Due to this assumption, in each time interval $\dot{v}(t_i) = 0$ except for $t_i = 0$ for which $\dot{v}(0)$ comes from the initial condition of the problem that is always set to 0. Differentiating with respect to time equation (7.15) once and twice we obtain respectively velocity and acceleration for the slip phase considered. The solution (7.15) holds up to the time instant in which the velocity vanishes again. At this point the algorithm checks if the mass is starting to move in the other direction or if it will retain its position. This task is performed comparing the actual external force applied with the maximum friction force available at the contact. Moreover, if the mass is in a phase of stick of finite duration, we evaluate the onset of slip looking for the time instant in which the external tangential force applied overcomes again the frictional force. Joining all the solutions, the complete response of the system to the applied loads is obtained.

7.4.2   The approximate solution for zero-stops

Den Hartog [90] and later Hong and Liu [91] give approximate formulas for the maximum displacement and velocity for a steady state non-sticking solution (i.e. 0 stop per cycle). Firstly in 1931, Den Hartog [90] proposed an approximation for the maximum displacement assuming that the trajectory in the phase and state plane is symmetric with respect to the x axis. More recently, in 2001, Hong and Liu [91] assumed that the trajectory is symmetric with respect to the origin, extended Den Hartog's results [90] obtaining the same formula for the maximum displacement, and a new formula for the maximum velocity:

$$v_{\max} = \sqrt{A^2 - \left[\frac{B\sin(\pi_1)}{\Omega(1 + \cos(\pi_1))}\right]^2} \tag{7.16}$$

$$\dot{v}_{\max} = |A|\,\omega_d\sqrt{1 - \left(\beta + \frac{k\Delta_1}{Q_1}\right)^2} +$$

$$+ \omega_n\sqrt{\frac{2B^2}{1 + \cos(\pi_1)} - \left(B - \beta A - \frac{\Omega^2\Delta_1}{1 - \Omega^2}\right)^2} \tag{7.17}$$

where $A = \frac{Q_1}{k(1-\Omega^2)}$, $B = \frac{fN_0}{k}$, $\pi_1 = \frac{\pi}{\Omega}$ and Δ_1 is the displacement at the time instant for which the maximum velocity is reached.

7.4.3   Time-marching algorithm

To check the results obtained eq. (7.14) is solved using a direct numerical integration. Different numerical methods are available to perform this task; we used the implicit Newmark method [110]. Briefly, this method assumes a form for the acceleration within the timestep, and integrating finds the resulting velocities and displacements:

$$\dot{v}_{i+1} = \dot{v}_i + \Delta t\left[(1 - \gamma)\ddot{v}_i + \gamma\ddot{v}_{i+1}\right] \tag{7.18}$$

$$v_{i+1} = v_i + \Delta t\dot{v}_i + \Delta t^2\left[\left(\frac{1}{2} - \delta\right)\ddot{v}_i + \delta\ddot{v}_{i+1}\right] \tag{7.19}$$

Using the parameters δ and γ respectively equal to 1/4 and 1/2 the method is unconditionally stable and conservative, thus no damping or excitation comes from the numerical integration. In each timestep, a "state" is assigned to the mass that indicates if the mass is in backward slip, forward slip or in stick. On the basis of the previous "state" of the mass the proper equilibrium equation is solved, and then the results are checked to ensure that they are coherent with the "state" guessed. If the results obtained are not coherent, a new state is assumed on the basis of the check result. The numerical simulation goes ahead up to the end of the temporal window considered, until the steady-state cycle is reached. It is assumed that the steady state condition is reached if for the last 2 cycles the dissipated energy per cycle is changed less then the 0.01%.

7.4.4   Results

To compare the solution obtained from a quasi-static analysis (QSTC) with that obtained from the dynamic one (DYN), in Figure 7.3 the two solutions (QSTC -DYN) for displacements are plotted with respect to time and in the phase and state plane, setting $\beta = 0.51$ and $\Omega = 0.05, 0.09, 0.47, 0.76$ respectively for the graphs (a-b), (c-d), (e-f), (g-h). Perhaps surprisingly, it should be remarked that a perfect match between QSTC and DYN solution is never obtained, because of the presence

of a certain number of stops in the DYN solution, which is evident particularly in the phase and state plane. Looking to the temporal evolution of displacements during the slip phase (see Figure 7.3 (a) and (c)) one can see that for the quasi-static solution a smooth curve links the two extended phases of stick (the displacement is sinusoidal for QSTC, see eqt.(7.6) and (7.3)), while the dynamic solution presents oscillations at the natural frequency during the slip phases, that in the most cases imply a state of stick for the mass (but not always). The phase and state plane (Figure 7.3 (b) and (d)) shows more clearly the stick-slip behavior of the dynamic solution, which results in a jumpy shape of the velocity. For small Ω, the dynamic and quasi-static displacement match, whereas, even for small Ω, the velocities seem to differ considerably. Upon increasing Ω, the maximum displacement and the maximum velocity in the dynamic solution grow up, and the number of stops obtained from the dynamic integration decreases. In particular the solutions reported in the Figure 7.3 (b-d-f-h) are respectively characterized by 10, 6, 2 and 0 stops. Notice that it is not possible to distinguish a solution with 2 stops (see Figure 7.3 (f)) with one with 0 stops (see Figure 7.3 (h)) looking only at the phase and state plane, as the shape of the solution remains the same. Vice versa, if one looks to the time evolution of displacements (see Figure 7.3 (e-g)) it is clear that when we have only 2 stops they are located in correspondence to the maximum positive and negative displacement where can be seen a plateau when the stop occurs. The DYN solution shape obtained is in agreement with that obtained by Hong and Liu in [91], who did not compare to the QSTC solution.
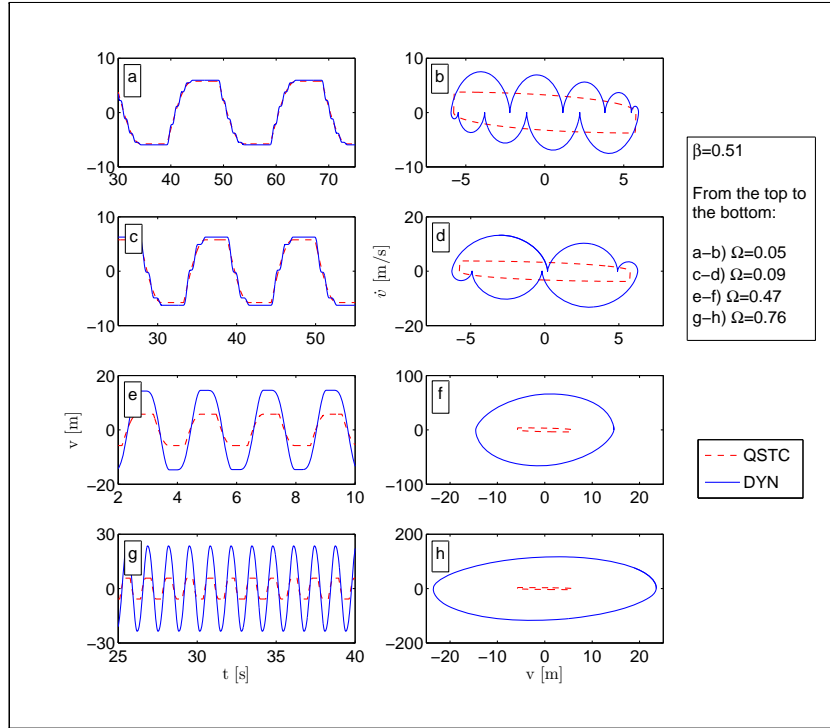
Fig. 7.3 On the left column: displacements (dashed line = QSTC solution, solid line = DYN solution) vs time. Right column: phase and state plane for (a-b) $\Omega = 0.05$, (c-d) $\Omega = 0.09$, (e-f) $\Omega = 0.47$, (g-h) $\Omega = 0.76$. All the simulations were run using $\beta = 0.51$. From the top to the bottom the solutions are characterized by 10 - 6 - 2 - 0 stops.

In order to assess whether a small amount of additional viscous damping in the system changes completely the behavior, Figure 7.4 shows results with 4 levels of damping factor ($\xi = \frac{c}{2\sqrt{km}} =$

$[0 - 0.15 - 1 - 3]$ respectively solid, dotted, dash-dotted, dashed thin line) compared with the no-damped QSTC solution (dashed thick line) for $\beta = 0.51$ and $\Omega = 0.05$. Only for a critical damping does the DYN solution get close to the no-damped QSTC limit.
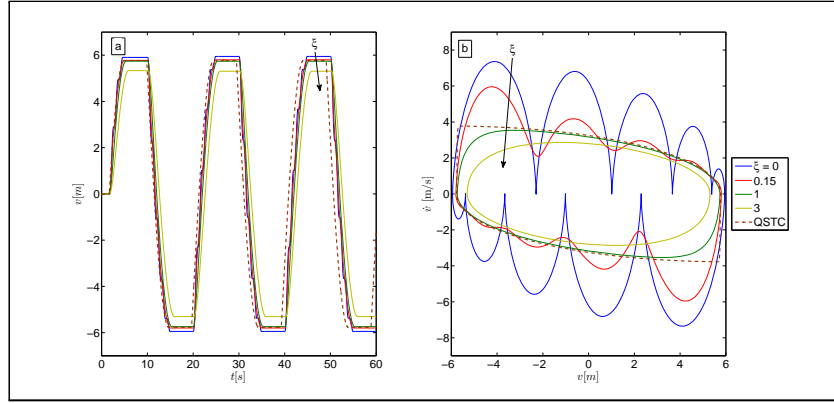
Fig. 7.4 Effect of additional viscous damping in the model. The viscous damping increases in this order solid, dotted, dash-dotted, dashed (thin) line compared with the no-damped QSTC solution (dashed thick line). Left column: displacements vs time. Right column: trajectory in the phase and state plane.

Having obtained that viscous damping alters the results qualitatively only for very high damping, we return in the following to the case of pure frictional damping. Similarly to Hong and Liu in [93], we run 5000 DYN simulations to characterize the number of stops per cycle of the solution as a function of Ω and β when the steady-state is reached. As the quasi-static limit requires a detailed analysis, the plane (Ω, β) is further subdivided into 2 grids. The first is characterized by 50 points for $\beta \epsilon [0.02, 0.98]$ and 50 for $\Omega \epsilon [0.02, 0.1]$, while for the second grid the interval for β remains the same but $\Omega \epsilon [0.1, 1.5]$. This choice gives us the possibility to directly compare our results to those proposed by Hong and Liu in ([93], [91]). In particular in this work a more complete pattern for $\beta \epsilon [0.02, 0.98]$ is provided that shows an herringbone distribution of stops for low Ω (see Figure 7.5 (a)).

In the range $\Omega \epsilon [0.1, 1.5]$ (see Figure 7.5 (b)) we found the area of 0 stop at the far right as found by Hong and Liu in [93] Fig. 7.8-7.9, but our results differ for the zone nearby. In fact, we always find a continuous transition in number of stops — from 0 stop in black to 2 stops per cycle in dark gray, and so on. Our results were verified carefully with the independent transient numerical solution – other small discrepancies with Hong and Liu results appear ([93], [91]) later in the region above resonance (leading even to a better comparison with the analytical solutions provided by those authors).
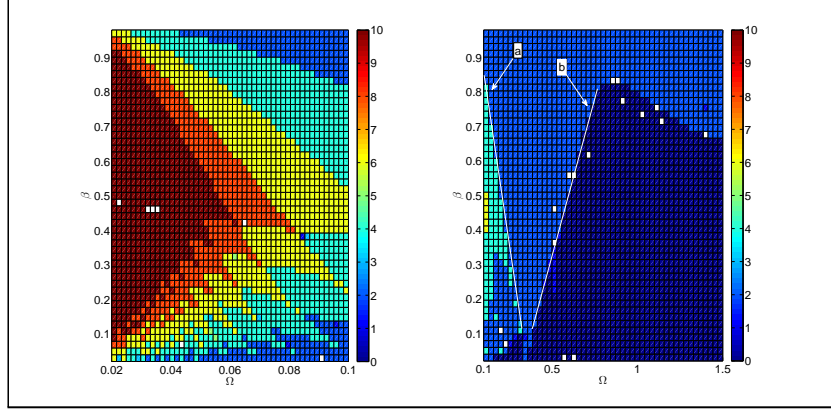
Fig. 7.5 Number of stops of the solution as a function of β and Ω. We set for β, 50 points ranging from 0.02 to 0.98; On the left side $\Omega \epsilon \left[0.02, 0.1\right]$, while on the right side $\Omega \epsilon \left[0.1, 1.5\right]$.

Making use of the piecewise analytical solution, the maximum displacement and the maximum velocity is computed when the steady state is reached. In Figure 7.6 (a) the maximum displacement (made dimensionless by Q_1/k, i.e. the frictionless maximum displacement) reached is plotted, for different value of the parameter β ranging from 0.1 to 0.9. When $\Omega \rightarrow 0$ each curve tends to $1 - \beta$, following a jumpy shape due to the fact that the number of stops of the solution changes, upon changing Ω^1. At a given value of Ω, the displacements start to increase markedly. Looking carefully, this seems to happen at the particular Ω for which the solution turns from 4 to 2 stops for the given value of β. The careful reader will note that we marked the limit using a white line, indicated as "a" in Figure 7.5 (b). For the highest values of β $(0.8 - 0.9)$, the resonance peak is completely erased due to the high damping introduced by the friction. Generally speaking, with this choice of dimensionless parameters, for a given Ω, the higher is β the lower is the maximum displacement reached.

In order to compare more effectively with the QSTC solution, in Figure 7.6 (b), the maximum displacement is made dimensionless by the quasi-static maximum displacement given analytically in (7.8). When Ω is sufficiently small, the quasi-static solution is approached and for all the values of β the curves go to 1 following the known jumpy shape. This dimensionless representation makes it clear that for the maximum displacement, the QSTC limit can be accepted. In general, the departure form the QSTC limit occurs at a larger value of Ω, the lower is β. This effectively introduces a pressure-dependence on the distance to the QSTC limit.

Turning back on a comparison with Hong and Liu [93], their Fig.13 shows results that are similar to our Fig. 7.6 (a) in the region of very low Ω. However, for higher Ω, we find smooth curves, whereas they continue to find bumps and discontinuous curves, even in the region above resonance for which the number of stops is zero both according to our and theirs results.

---

[1]The jumps in the results of steady state amplitude of motion seem to happen for any value of β and hence are not associated to "high friction" and multiplicity of quasi-static solutions (see Klarbring, [95], [96]) which is generally related to the presence of off-diagonal stiffnesses, which is not the case here. It seems more like a jump phenomena typical of non-linear systems, involving discontinuous and significant changes in the response of as some forcing parameter is slowly varied — in this case, due to the change of number of stops in the solution. A different "jump" is the change of slope in the displacement amplification for high β for a certain frequency, which correspond to a "damped" resonance similar to what happens with an oscillator with viscous damping.

Fig. 7.6 On the left side the maximum displacement made dimensionless by Q_1/k; On the right
side the maximum displacement made dimensionless by the quasi-static one $v_{qstc}|_{\max}$.

Moving to a comparison for the velocities, in Figure 7.7 (a) we plot the maximum velocity as
a function of Ω made dimensionless with $\omega_d Q_1/k$, i.e. the quasi-static frictionless amplitude for
velocity, for different β. For $\Omega \to 0$ each curve tends to a value below 2. Notice that this ratio
is more or less constant up to a certain Ω, between 0.5 and 0.8 in the case of the Figure. For
even larger Ω, the dynamic effects show up considerably up to the resonance peak. If we compare
carefully the curves for $\beta \epsilon [0.1 - 0.7]$, we will see that those dynamic effects show up when the
dynamic solution enters in the field of 0 stop, i.e. black region in Figure 7.5 (b) (the line "b"
indicates the limit). Starting from $\beta = 0.7$ the friction force is high enough to reduce markedly
the maximum velocity. Notice that at $\Omega = 1.5$ all the curves are below 1.

In order to elucidate more specifically the QSTC limit, in Figure 7.7 (b) we plot the maximum
velocity made dimensionless with the quasi-static value (7.12). Notice that this change doesn't
affect the curves for $\beta < 0.5$ since the QSTC limit corresponds exactly to the frictionless solution.
With this dimensionless formulation, for $\Omega \to 0$ the curves are closer and tend to a factor that is
comprised between $1.5 - 2$ for all the curves. The discrepancy between the QSTC limit and the
DYN solution was already remarked in the previous paragraph and Figure 7.3 (a-b-c-d) and in
particular (b) and (d). Strictly speaking, the 10% rule of Brake and Hills [92] cannot be applied
in the present context.

Finally, in comparison with the results of Hong and Liu [93] (specifically, their Fig.13), our
results are again in agreement in the low region of Ω, but, similarly to the displacements, there
are discrepancies at intermediate and high Ω for low β where they find jumpy curves, whereas our
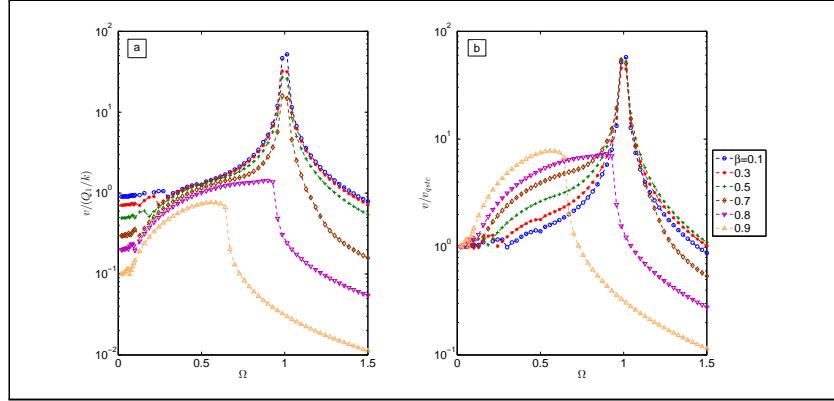results are smooth and continuous.
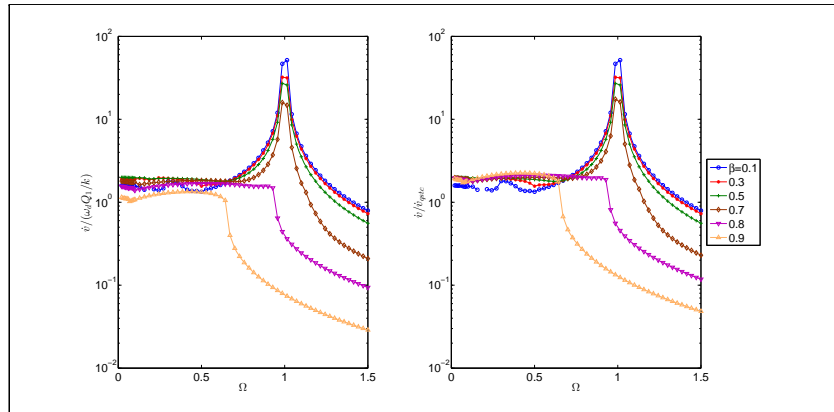
Fig.7.7 On the left side the maximum velocity made dimensionless by $(\omega_d Q_1/k)$; On the right side the maximum velocity made dimensionless by the quasi-static one $\dot{v}_{qstc}\big|_{\max}$.

Finally, we shall not present results for energy dissipation in the joint, since, for normal constant load, these are proportional to the displacements.

Due to the discrepancies in displacements and velocities with those obtained by Hong and Liu [93], we further carefully checked the results obtained with our piecewise analytical solution using the time-marching numerical algorithm — finding out that correspond more closely to the Den Hartog [90] and Hong and Liu [91] own estimates eqt. (7.16)-(7.17) in the region where we expect 0 stops. In Figure 7.8-7.9, the result of the comparison is plotted: it is fair to say that the displacements compare favorably each other for all the values of β used, while looking to Fig. 4 in Hong and Liu paper [91] one can see that they don't find a good match, in particular for low β (i.e. $1/\alpha$ in Hong's papers [93],[91]) where the bumpy shape appears. In Fig. 7.9, we compare the maximum velocity for different β. In this case we obtain a good match for $\beta \epsilon\, [0.1 - 0.2 - 0.3 - 0.4]$, whereas in Figure 7 of Hong and Liu [91] there are differences. Finally, some discrepancies appear for $\beta = [0.5 - 0.6]$ in the zone above the resonance, also found by Hong and Liu [91]. This is due evidently to the simplifications in the shape of the solution trajectory.

The solution with the fully transient time-marching algorithm also permitted to explore if non-periodic solutions could emerge, since they are in principle also possible: however, we did not find evidence of non-periodic solutions.
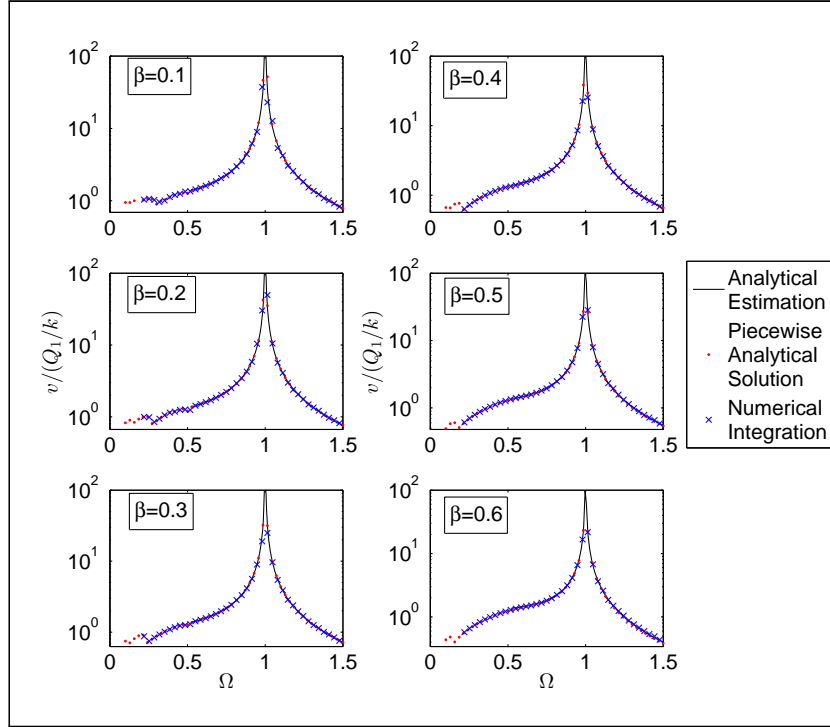
Fig. 7.8 Dimensionless maximum displacement obtained using the Den Hartog estimation (solid line), piecewise analytical solution (dots) and the time-marching algorithm (cross).
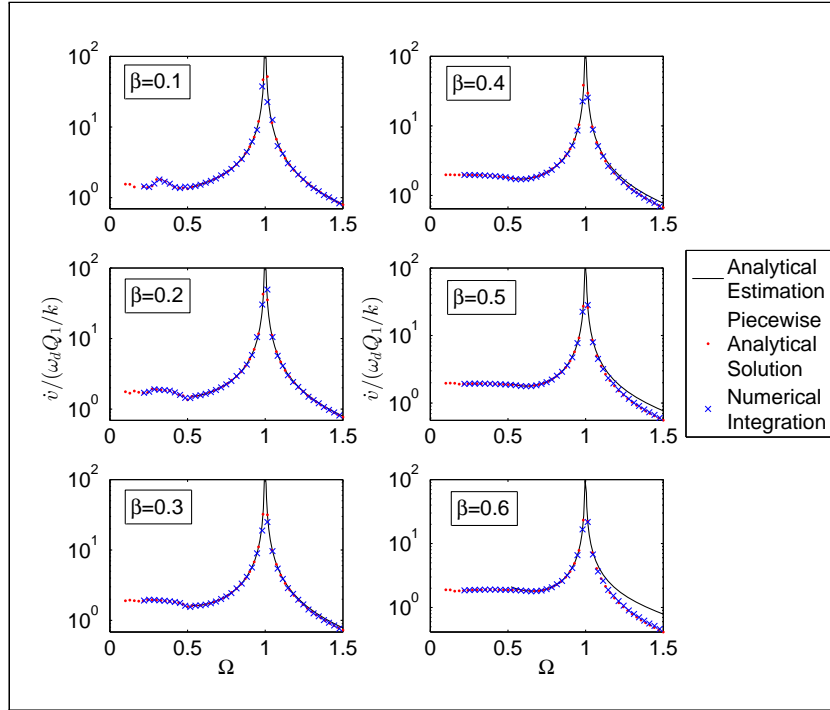
Fig. 7.9 Dimensionless maximum velocity obtained using the Hong and Liu estimation (solid line), the piecewise analytical solution (dots) and the time-marching algorithm (cross).

7.5   Normal load variation effects on vibration amplitude and dissipation

7.5.1   The model

In the first part of this chapter the behavior of a single degree of freedom damped with Coulomb friction has been studied with the hypothesis that the tangential load is harmonic and the normal load is kept constant. Here it is assumed that both the variation of normal and tangential load is harmonic (Fig. 7.10), which yields

$$N(t) = N_0 + N_1 \sin(\omega_d t + \delta) \tag{7.20}$$
$$Q(t) = Q_1 \sin(\omega_d t) \tag{7.21}$$

where $N_0, N_1 > 0$ are constant and amplitude coefficients of the normal load, and $Q_1 > 0$ is the amplitude of tangential load. δ is the phase shift of the normal load. Finally, ω_d is the angular frequency of the loading.

It is convenient to introduce a new dimensionless parameter η (besides β)

$$0 < \eta = \frac{N_1}{N_0} < 1 \tag{7.22}$$

To avoid contact separation η was assumed to be less than unity in eq. (7.22). Contact separation will involve impact and it is most likely that engineering judgement suggests to avoid this range, particularly as friction damper. To avoid "shakedown" of the system, the simple condition $\beta < 1$

holds in the case of constant normal load, whereas we will find a β_{cr} value more in general in a later paragraph.

The case considered by Hong & Liu [93],[91] corresponds to $\eta = N_1 = 0$ and hence here we have 2 additional parameters (η, δ).
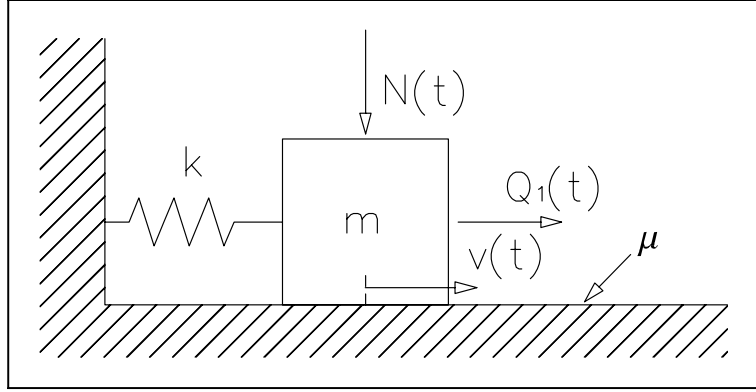
Figure 7.10 Harmonic oscillator damped by Coulomb friction

7.5.2   In phase loading

Hereafter, we follow again the argument presented by Jang and Barber [97] for the quasi-static behavior of the system with $\delta = 0°$, to set the scene for the more general case. Jang and Barber in [97] considered the loading (7.20, 7.21) where the periodic function is a more general $-1 \le g(t) \le 1$. The case $g(t) = \sin(\omega_d t)$ is considered, but we maintain the notation of [97] to make a comparison easier.

First, consider the mass is sliding towards the positive direction. According to equilibrium in the quasi-static case (no inertia)

$$Q_1 \sin(\omega_d t) - f\left[N_0 + N_1 \sin(\omega_d t)\right] - kv(t) = 0 \tag{7.23}$$

and hence

$$v(t) = \left(\frac{Q_1 - fN_1}{k}\right)\sin(\omega_d t) - \frac{fN_0}{k} \tag{7.24}$$

where $v(t)$ is the displacement of the mass according to the system of reference in Fig. 7.10. The maximum positive displacement will be reached when $\sin(\omega_d t)$ will reach its maximum value, so

$$\widetilde{v}_{\max} = 1 - \beta(1 + \eta) \tag{7.25}$$

where the dimensionless displacement $\widetilde{v} = \frac{v}{Q_1/k}$ has been introduced. Rewriting the equilibrium in the case in which the mass is moving towards the negative direction, the minimum displacement is reached when $\sin(\omega_d t)$ reaches its minimum value -1, so

$$\widetilde{v}_{\min} = -\left[1 - \beta(1 - \eta)\right] \tag{7.26}$$

The absolute maximum displacement is then the largest in modulus, and this happens to be $\widetilde{v}_{\min}$(keep in mind that for in phase loading $0 \le \beta < 1$)

$$\widetilde{v}_{\max} = \max(\left|\widetilde{v}_{\max}\right|, \left|\widetilde{v}_{\min}\right|) = \left|\widetilde{v}_{\min}\right| = 1 - \beta(1 - \eta) \tag{7.27}$$

Also, from (7.25) and (7.26), the dimensionless amplitude of displacement

$$\widetilde{v}_a = \frac{\widetilde{v}_{\max} - \widetilde{v}_{\min}}{2} = 1 - \beta \tag{7.28}$$

which does not depend on η.

It is possible to estimate also the velocity and the velocity peak, which results after some algebra in

$$\left| \dot{\widetilde{v}} \right|_{\max} = \begin{cases} 1 + \beta\eta & \text{for } 0 \leqslant \beta \leqslant \frac{1}{2+\eta} \\ 2\sqrt{\beta\left(1-\beta\right)\left(1+\eta\right)} & \text{for } \frac{1}{2+\eta} \leqslant \beta \leqslant 1 \end{cases} \tag{7.29}$$

Moving to energy dissipation, for in phase loading Jang and Barber in [97] already found

$$\widetilde{W}\big|_{\delta=0°} = \left.\frac{W}{fN_0\frac{Q_1}{k}}\right|_{\delta=0°} = 4\frac{\left(1-\beta\right)\left(1-\beta\eta^2\right)}{1-\beta^2\eta^2} \tag{7.30}$$

7.5.3   Quadrature loading

Here some formulas for the case of quadrature loading ($\delta = 90°$) are reported, while the most general case is treated in Appendix B. Quadrature loading can occur whenever there is an eccentric rotating mass, and loosely speaking, it can also correspond to small imperfections in the symmetry of rotating systems, including gas turbines (mistuning).

Following the analysis in Appendix B, the maximum dimensionless displacement is equal to

$$\widetilde{v}_{\max}\big|_{\delta=90°} = \sqrt{1 + \beta^2\eta^2} - \beta \tag{7.31}$$

which, due to symmetry, coincides with the displacement amplitude. Notice that, contrary to the in phase loading case, there is dependence on η.

The maximum velocity is given by

$$\dot{\widetilde{v}}_{\max}\big|_{\delta=90°} = \begin{cases} \sqrt{1 + \beta^2\eta^2} & \text{for } \beta \leqslant \beta_1 \\ 2\sqrt{\beta\sqrt{1+\beta^2\eta^2} - \beta^2} & \text{for } \beta > \beta_1 \end{cases} \tag{7.32}$$

where $\beta_1 = \frac{1}{\sqrt{4-\eta^2}}$.

A simple formula for dissipation (B.31) is also derived in Appendix:

$$\widetilde{W}\big|_{\delta=90°} = \left.\frac{W}{fN_0\frac{Q_1}{k}}\right|_{\delta=90°} = 4\left(\frac{\sqrt{1+\beta^2\eta^2} - \beta}{1+\beta^2\eta^2}\right) \tag{7.33}$$

which, together with the case $\delta = 0°$ was covered by Jang and Barber [97], permits to have a clear idea of the most important regimes. In fact systems which experience quadrature loading are widely spread, for example machine excited by a rotating eccentric mass.

7.5.4   The shakedown limit

The SDOF oscillator in Fig. 7.10 will reach a "shakedown state", a steady-state stick condition, in case where there is a possible such state. This is because this system has no coupling between tangential displacements and normal load, and will obey Melan's theorem [98]([2]), that is, a final state of shakedown will be reached, if there is one. Writing the condition for shakedown

---

[2]Strictly speaking, the theorem has been proved only under quasi-static conditions.

$$|Q_1 \sin(\omega_d t) - kv(t)| \leq f\left[N_0 + N_1 \sin(\omega_d t + \delta)\right] \quad , \forall t \tag{7.34}$$

and rearranging

$$-\beta + \sqrt{1 + \beta^2 \eta^2 - 2\beta\eta \cos(\delta)} \leq \widetilde{v}(t) \leq \beta - \sqrt{(1 + \beta^2 \eta^2 + 2\beta\eta \cos(\delta))} \rightarrow \tag{7.35}$$

where the condition

$$\beta \geq \sqrt{\frac{1 - \eta^2 \cos^2(\delta)}{1 - \eta^2}} = \beta_{cr} \tag{7.36}$$

ensures that a shakedown solution exist. For $\delta = 0°$, and any normal load variation, $\beta_{cr} = 1$.

Fig. 7.11 plots $1/\beta_{cr}$ as a function of η for $\delta \epsilon \left[0°, 30°, 60°, 90°\right]$. For $\delta > 0°$, the factor β_{cr} increases always up to infinity for $\eta = 1$. The highest values of β_{cr} are obtained for quadrature loading, corresponding to the fact that shakedown is obtained with much higher normal loads.
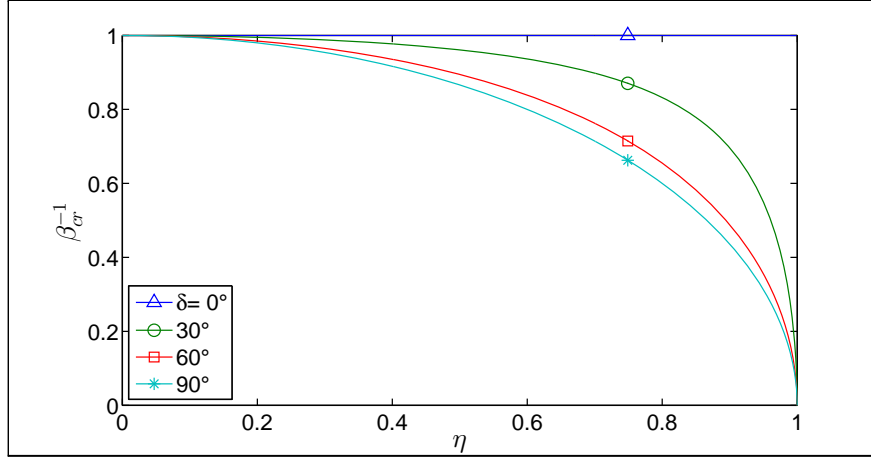
Figure 7.11 β_{cr}^{-1} plotted against η for the following $\delta = [0°, 30°, 60°, 90°]$

7.5.5   The dynamic solution

Consider that the system sketched in Fig. 7.10 is in a phase of slip; from the linear momentum balance in the horizontal direction

$$m\ddot{v}(t) + kv(t) = Q_1 \sin(\omega_d t) - sign(\dot{v})f\left[N_0 + N_1 \sin(\omega_d t + \delta)\right] \tag{7.37}$$

where $v(t)$ is the position of the mass at the time t. We subdivide our temporal window in intervals in which the mass is in stick or in slip. For the first case (stick), the solution of the problem is trivial, while for the slip phase we need to solve (7.37). Notice that the mass could turn from a forward slip phase both to a backward slip phase and to a stick phase. In both those cases, there will be a time instant in which the velocity vanishes. To simplify the solution of the problem, we look for a piecewise analytical solution for which, in each interval considered, the velocity retains the same sign. Under the latter hypothesis, the (7.37) is a linear, second order ODE thus making use of the superposition principle and summing up the transient and the steady-state solutions we obtain

$$v(t) = v(t_i) - \left[v(t_i) + sign(\dot{v})\frac{fN_0}{k} \right] \{1 - \cos\left[\omega_n\left(t - t_i\right)\right]\} +$$

$$+ \frac{\dot{v}(t_i)}{\omega_n} \sin\left[\omega_n\left(t - t_i\right)\right] +$$

$$+ \frac{Q_1}{k\left(1 - \Omega^2\right)} \{\sin(\omega_d t) - \sin(\omega_d t_i)\cos\left[\omega_n\left(t - t_i\right)\right] +$$

$$-\Omega\cos(\omega_d t_i)\sin\left[\omega_n\left(t - t_i\right)\right]\} +$$

$$+ sign(\dot{v})\frac{fN_1}{k\left(1 - \Omega^2\right)} \{\sin(\omega_d t_i + \delta)\cos\left[\omega_n\left(t - t_i\right)\right] +$$

$$+\Omega\cos(\omega_d t_i + \delta)\sin\left[\omega_n\left(t - t_i\right)\right] - \sin\left(\omega_d t + \delta\right)\} \tag{7.38}$$

where $\omega_n = \sqrt{k/m}$, $\Omega = \omega_d/\omega_n$, $v(t_i)$ and $\dot{v}(t_i)$ the initial conditions. Differentiating with respect to the time equation (7.38) once and twice, respectively velocity and acceleration are obtained for the slip phase considered. The solution (7.38) holds up to the time instant in which $\dot{v}(t) = 0$. At this point the algorithm needs to check if the mass is starting to move towards the other direction or if it will retain its position. This task is performed comparing the actual external force applied with the maximum friction force available at the contact. If the mass is in phase of stick we evaluate the onset of slip looking for the time instant in which the external tangential force applied overcomes the frictional force. Joining all the solutions found the complete response of the system is obtained to the applied loads.

With the aim to check the results obtained with the semi-analytical solution, we have solved (7.37) also using a direct numerical integration by an implicit Newmark method.

7.5.6   Results

It is impractical to give results for the entire range of possible parameters, since there are 4 of them: $\beta, \delta, \eta, \Omega$. In Fig. 7.12, we give for example some results for the displacement amplitude $\tilde{v}_a$ for a case with low or high pressure $\beta = 0.2$ (a,c), 0.9 (b,d) and either in phase loading $\delta = 0°$ (a,b) or quadrature $\delta = 90°$ (c,d). The results show that the effect of normal load variation is very small in the $\beta = 0.2$ case, and the response is unbounded. On the other hand for $\beta = 0.9$ the effect of the normal load variation is important, in particular in the zone before the resonance for $\delta = 0°$ and for all frequencies Ω for $\delta = 90°$. Notice that for $\delta = 0°$ the quasi-static limit predicted no effect of the normal load variation η, whereas the dynamic model shows a significant dependence at intermediate frequencies. Also, for $(\beta, \delta) = (0.9, 90°)$ (see Fig. 7.12 (d)) an increasing trend of $\tilde{v}_a$ with η for all Ω is obtained.
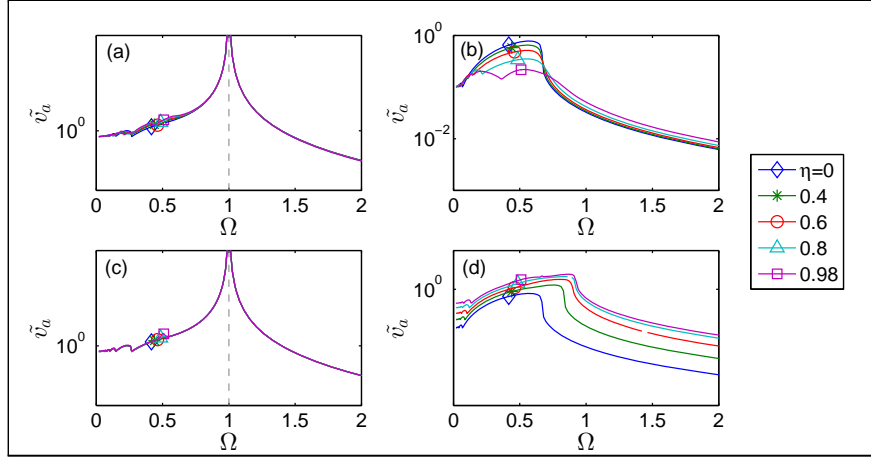
Figure 7.12 Dimensionless displacement amplitude for $\beta = 0.2$ (a,c), $\beta = 0.9$ (b,d) and either in phase loading $\delta = 0°$ (a,b) or quadrature $\delta = 90°$ (c,d).
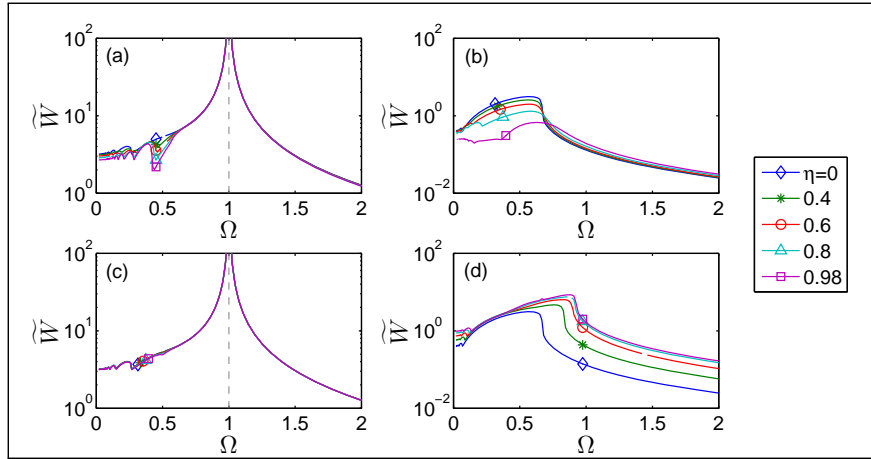
Figure 7.13 Dimensionless dissipation for $\beta = 0.2$ (a,c), $\beta = 0.9$ (b,d) and either in phase loading $\delta = 0°$ (a,b) or quadrature $\delta = 90°$ (c,d).

In Fig. 7.13 the dimensionless dissipation per cycle is plotted which shows a similar behavior with respect to displacement. Moreover, since even in the in-phase loading case, the quasi-static prediction shows here a dependence on normal load variation, the difference between quasi-static and dynamic prediction is somehow smaller.

The effect of normal load variation is important only at high β values (see Fig. 7.12-13), while for small amplitude of tangential force Q (small β) the effect is negligible. In Fig. 7.14 the frequency response function of the system is plotted for $\eta = 0.9$ and $\beta = [0.2, 0.4, 0.6, 0.7, 0.8, 0.9]$ respectively for in-phase loading (a) and quadrature loading (b). The figures show that the normal load variation and its phase are important approximately for $\beta \gtrsim 0.7$.
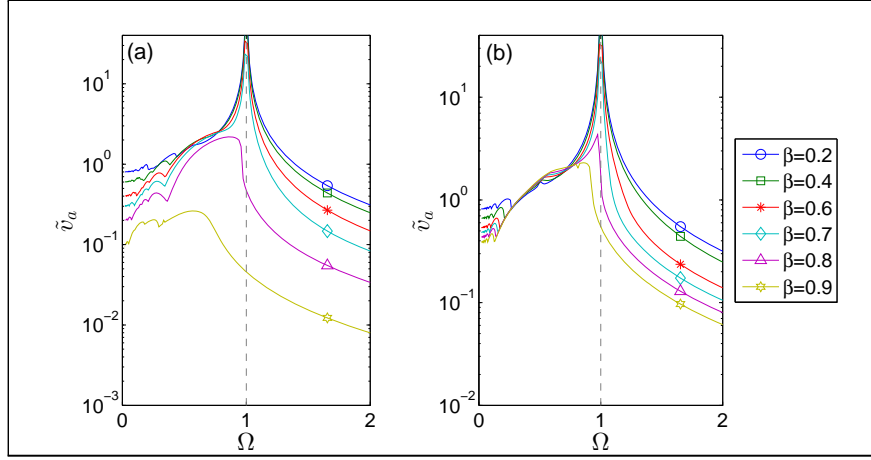
Figure 7.14 Dimensionless displacement amplitude for $\beta = [0.2, 0.4, 0.6, 0.7, 0.8, 0.9]$ and $\eta = 0.9$. (a) in phase loading $\delta = 0°$ (b) quadrature loading $\delta = 90°$.

Given the best use of frictional dampers is a regime where the displacement is bounded, we shall concentrate in this region: first, we find the range of parameters to obtain this regime in the following paragraph.

7.5.7   Bounded response regime

Optimal damping is achieved by making sure the displacement is bounded in the entire frequency range, and that it is the smallest possible value. In the present simple system without damper stiffness, the model predicts obviously a full stick condition which is trivially "optimal", involving no displacement and no dissipation at all. But this is a limit of the simplification in the model, as with a finite damper stiffness, too high normal load implies the resonance of the system with the two spring in parallel — possibly implying an infinite peak in the response again. Hence, we can have an idea of the "optimal" regime by looking at the range of normal loads for which there is some slip, but for which the response of the system is bounded. For constant normal load, this is ([100], [99]) $\pi/4 < \beta < 1$. For a general out-of-phase loading we compute the maximum displacement amplitude changing β for all the range of Ω, and collect all the results in Fig. 7.15 for in phase loading (a) and quadrature loading (b). The results obtained indicate the same inferior boundary ($\beta = \pi/4 \simeq 0.78$) for both the case in phase (Fig. 7.15 (a)) and quadrature (Fig. 7.15 (b)) loading, to have a bounded solution, as it is for normal constant load. We checked this limit even for $\delta = [30° - 60° - 120° - 150°]$, thus we deduce that it should be a general feature of such a system. The superior boundary (corresponding to shakedown limit) for $\delta = 0°$ is $\beta > 1$ (see Fig. 7.11), while for $\delta = 90°$ it is a function of η, as shown in Fig. 7.11.
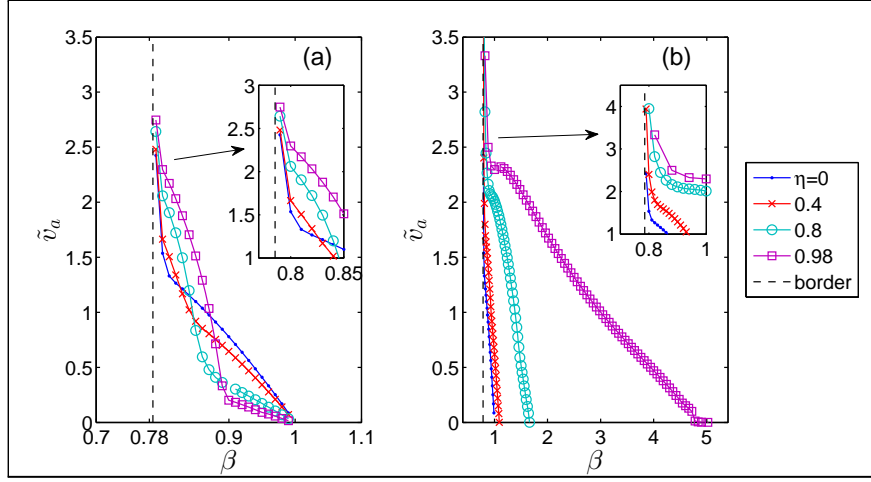
Figure 7.15 Dimensionless displacement amplitude vs β for in phase loading (a), and quadrature loading (b).

For in phase loading, there is a first range for low β (about $0.78 \lesssim \beta \lesssim 0.85$) for which the amplification increases with η, and a second range (for $0.85 \lesssim \beta \lesssim 1$), for which the amplification decreases with η. This second regime is most interesting for optimal dampers design. Notice that the static prediction was $1 - \beta$, independent on η, which is very close to the dynamic result when β is high. For quadrature loading, higher η yields higher amplification.

Comparison with quasi-static solution

For the quasi-static prediction, the amplitude of displacements, with respect to the case with constant normal load, can be obtained from the formulae above in closed form for in-phase and quadrature loading, (7.28), (7.31), as

$$\left.\frac{\widetilde{v}_a}{\widetilde{v}_{a,\eta=0}}\right|_{\delta=0°} = 1 \tag{7.39}$$

$$\left.\frac{\widetilde{v}_a}{\widetilde{v}_{a,\eta=0}}\right|_{\delta=90°} = \frac{\sqrt{1+\beta^2\eta^2}-\beta}{1-\beta} \tag{7.40}$$

Given the bounded response dynamic regime has a finite peak amplitude, it would be interesting to see if the dependence on the various parameters is similar to the quasi-static model.
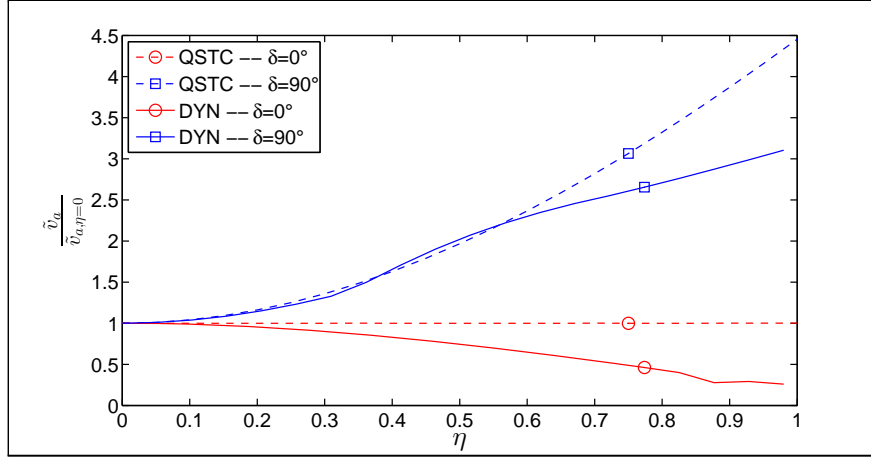
Figure 7.16 $((v_a^\delta)/(v_{a,\eta=0}^\delta))$ i.e. the ratio between the dimensionless displacement amplitude and the respective but with constant normal load, for $\delta = 0°$ (circle) and $\delta = 90°$ (square). In both cases $\beta = 0.9$. The dotted line refers to the quasi-static case, the solid line to the dynamic.

In Fig. 7.16, the peak of displacement amplitude is plotted divided by the respective case but with constant normal load. We used dashed lines for the Quasi-STatiC case and solid line for the full DYNamic results. Fig. 7.16 shows the effect of normal load is an amplification of vibrations for the case of $\delta = 90°$ and a decrease for $\delta = 0°$, which was unexpected from the quasi-static prediction. In particular, the maximum vibration amplitude reduction to about 0.25, while the maximum increment is about 3.

If the same arguments are repeated for the frictional energy dissipation, from (7.30) we obtain

$$\left.\frac{\widetilde{W}}{\widetilde{W}_{\eta=0}}\right|_{\delta=0°} = \frac{1-\beta\eta^2}{1-\beta^2\eta^2} \qquad (7.41)$$

which decreases with η. Also, for $\delta = 90°$ (eq. (7.33))

$$\left.\frac{\widetilde{W}}{\widetilde{W}_{\eta=0}}\right|_{\delta=90°} = \frac{1}{1-\beta}\frac{\sqrt{1+\beta^2\eta^2}-\beta}{1+\beta^2\eta^2} \qquad (7.42)$$
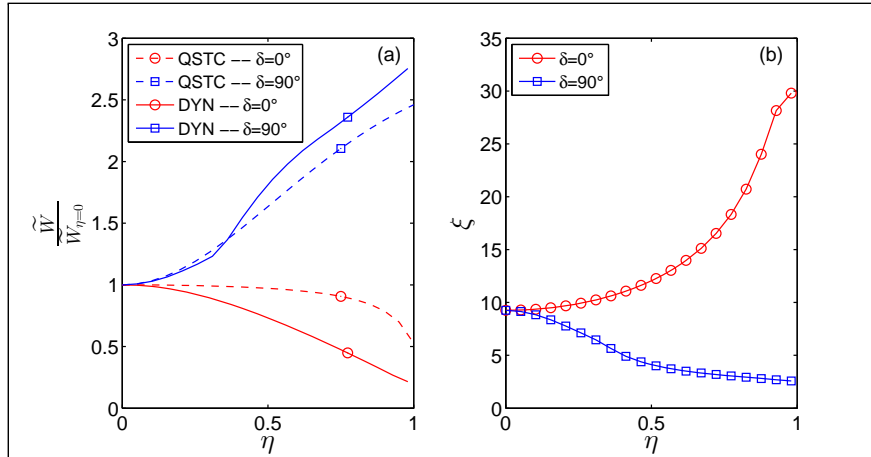
Figure 7.17 (a) $\widetilde{W}_\delta / \widetilde{W}_{\delta,\eta=0}$ i.e. the ratio between the dimensionless dissipation and the respective
but with constant normal load. The dotted line refers to the quasi-static case, the solid line to
the dynamic. (b) The loss factor $\xi = W/\frac{1}{2}kv_a^2$ versus η. In both (a)-(b) $\beta = 0.9$, and $\delta = 0°$
(circle), $\delta = 90°$ (square).

Fig. 7.17 (a) plots the amplification of dissipation with respect to the constant normal load
case, for both quasi-static and dynamic models. In this case, contrary to the displacements, the
trends of the two models are similar. Dissipation increases for the case $\delta = 90°$ up to a factor
~ 2.5 while it decreases to a factor ~ 0.2 for in-phase loading.

To better compare the damping efficiency of the system, the loss factor ξ, (i.e. the ratio between
the dissipated energy W and the maximum elastic energy stored in the spring during the vibration
$E_k = \frac{1}{2}kv_a^2$) is plotted in Fig. 7.17 (b). The result plotted against η for both in-phase and
quadrature loading confirms that the in-phase case is favorable.

7.6   Conclusions

In this chapter, we studied the dynamics of the elementary frictional system made of a concentrated
mass that slides against a frictional plane loaded by a periodic tangential force. In the first the
normal has been considered constant, and the limit towards zero loading frequency has been
investigated comparing with the solution obtained neglecting the mass (QSTC approximation). It
was found that the maximum displacement is given correctly by the QSTC approximation, and
this holds up to frequencies when the dynamic solution is characterized by more then 2 stops.
Interestingly this may sound counterintuitive as the QSTC solution per se contains only 2 stops.
As regards the maximum velocity, in a dynamic solution it never matches the QSTC limit, due
to the multiple stops in the low frequency end. However, there is a ratio between the QSTC and
the DYN maximum velocity that remains nearly constant up to a certain frequency ($\Omega \simeq 0.6$, for
$\beta < 0.9$), but again this depends on the pressure level, i.e. on β. We show that *further* dynamic
effects show up when the solution turns from 2 to 0 stop per cycle. If significant additional viscous
damping is added, it suppresses stick-slip and for values of the order of critical damping ratio, the
DYN solution is close to the QSTC limit.

In the second section of the chapter harmonic varying normal and tangential forces, with relative
phase, have been considered. It was shown that dissipation can be much higher for quadrature
loading, as noticed also by Jang and Barber [94] for the model under quasi-static loading. However,
in terms of "vibration", this does not correspond to higher "damping" of vibrations for our system.
The regime of "bounded" response of the system, which is given by $\beta \geq \pi/4$ as for the case of
constant normal load, has been studied. For in-phase loads, variation of normal load can lead to a
large reduction of both dissipation and displacement, and this is not expected from the quasi-static
prediction. These results are relative to a very simplified model, and hence, definitive indications
on the optimal design of dampers are not possible within this analysis.

Chapter 8

Dynamical behaviour of a linear oscillator coupled with a massless Coulomb damper

In the previous chapter we have studied the dynamical behaviour of a simple Coulomb frictional oscillator under both a constant and tangential normal load. Due to the high simplifications adopted no firm conclusion could be gained about damper design. Here we consider a lumped structure (mass spring damper model) that is elastically coupled to a massless damper. Particularly we will consider the case of wedge shaped frictional dampers which are widely used in civil, mechanical and aeronautical engineering with the purpose to limit and damp vibrations, increase component fatigue-life, or resist seismic loads. The wedge shape obviously couples normal and tangential loads, which complicates the analysis. The model adopted can be considered a generalization of the Griffin model, originally devised for underplatform dampers in turbine blade attachments. It is found that the damper is more effective when normal and tangential loads vary in-phase.

8.1 Introduction

Wedge shaped Coulomb dampers are often used not because it is considered to be superior in dissipating energy, but because it can be convenient for practical reasons: stability, self-aligning capabilities, self-locking etc. In the EDR seismic dampers [101] (Fig. 8.1 (a)), the wedges are easily included in helicoidal springs and a variable normal load is induced, linearly with the tangential displacement of the structure during the loading phase, and in fact more suddenly decreasing during the unloading phase, giving a triangular hysteresis loop. Sometimes [102], friction-variable characteristics of the device are obtained. In railways, wedge shaped dampers are used in suspension systems ([103], [104], [105]), and in aeronautical engineering examples are the underplatform frictional dampers used in gas turbines (Figure 8.1 (b), [106], [107], [108], [109]). In more general mechanical engineering joints, and many frictional interfaces, frictional damping is a primary source of damping, often greater than the internal damping in the materials.
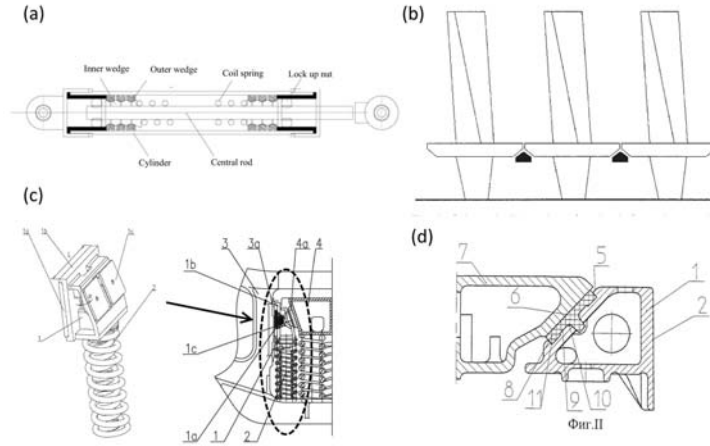
Figure 8.1 (a) Energy Dissipating Restraint from [102] (b) Underplatform dampers from [106] (c) Friction shock absorber for railway car truck from [105] (d) Damping device for railway car truck from [104]

A simple but effectively lumped system was studied by J. H. Griffin [108] with the underplatform dampers application in mind. It consists (see Fig. 8.2) of a mass-spring-dashpot system to model the structure, and a spring linked to a massless Coulomb damper to model the contact interface on which a constant normal load is applied (because the damper itself has inertia force due to the constant centrifugal field).

In this chapter we further explore the effect of a variable normal load in damping vibration in such a simple model, modified in that the wedge shape induces a coupling of normal and tangential load variations. In particular, we introduce a sinusoidal variation of the normal load with an arbitrary phase shift with respect to the tangential load applied to the structure. The in phase loading and the quadrature loading are analyzed more in detail with a comparison to the quasi-static solution of the problem.

8.2   The model

The model used is sketched in Fig. 8.2. The mass m, the stiffness k and the damping coefficient c take into account respectively of an equivalent inertia, stiffness and damping of the structure considered, while the damper is considered massless and is linked to the mass via a contact stiffness k_d. This model has two degrees of freedom: $v(t)$ is the horizontal displacement of the mass and $y(t)$ is the damper displacement, both are taken positive towards the right as shown in Fig. 8.2.
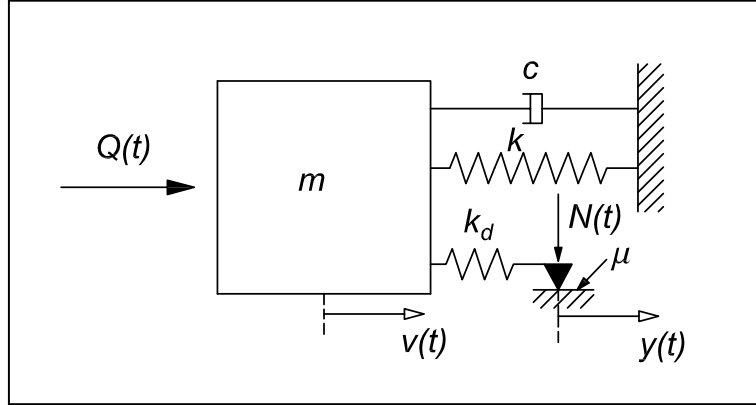
Figure 8.2 Single Degree Of Freedom (DOF) model coupled with a massless Coulomb damper (Griffin model), where the normal load $N(t)$ is made variable.

Consider a normal and tangential load of the form

$$N(t) = N_0 + N_1 \sin(\omega_d t + \delta) \tag{8.1}$$
$$Q(t) = Q_1 \sin(\omega_d t) \tag{8.2}$$

$N(t)$ is the normal force applied to the damper, $Q(t)$ is the tangential force applied to the mass. The loads have the same frequency ω_d, but the normal load has a mean component N_0, a sinusoidal amplitude N_1 and a general phase shift δ with respect to the tangential load, which has only the sinusoidal component Q_1. It is useful to introduce two dimensionless parameters

$$\beta = \frac{f N_0}{Q_1} > 0 \tag{8.3}$$

and

$$0 < \eta = \frac{N_1}{N_0} < 1 \tag{8.4}$$

The upper bound introduced for η guarantees that no separation occurs. Amonton-Coulomb model is used for dry friction (8.5) with no difference between the dynamic and the static friction coefficient f

$$\begin{cases} F(t) = -\dfrac{\dot{y}(t)}{|\dot{y}(t)|} f N(t) & \dot{y}(t) \neq 0 \\ \quad F(t) \leq |f N(t)| & \dot{y}(t) = 0 \end{cases} \tag{8.5}$$

8.3 The dynamic solution

8.3.1 Direct numerical integration

We integrate numerically the equation of motion using the Newmark method [110] with the parameters θ and γ respectively equal to $1/4$ and $1/2$. This choice makes the method unconditionally stable and conservative, thus no damping or excitation comes from the numerical integration. Specifically, mass velocity and displacement for the step $i+1$ are evaluated as follow

$$\dot{v}_{i+1} = \dot{v}_i + \Delta t \left[(1 - \gamma) \ddot{v}_i + \gamma \ddot{v}_{i+1} \right] \tag{8.6}$$

$$v_{i+1} = v_i + \Delta t \dot{v}_i + \Delta t^2 \left[\left(\frac{1}{2} - \theta \right) \ddot{v}_i + \theta \ddot{v}_{i+1} \right] \tag{8.7}$$

In each timestep, a "state" is assigned to the damper which gives the rule to compute the force that the damper transmits to the mass $F_{d \to m}$

$$F_{d \to m} = \begin{cases} -k_d \left(v(t) - \overline{y} \right), & \dot{y} = 0 \\ -sign(\dot{y}) f N(t), & \dot{y} \neq 0 \end{cases} \tag{8.8}$$

where $\overline{y}$ is the last stuck position of the damper. Clearly, this equation simply says that the possible states are only three: stick or slip (backward or forward slip), as separation is avoided. The results of each timestep are checked to ensure that they are coherent with the guessed "state". If the results obtained are not coherent, a new state is assumed. The numerical integration goes ahead until a steady-state condition is reached: within the last 3 loading cycles the dissipated energy per cycle, the root mean square for mass and damper displacement should change less than 0.1%.

8.3.2   Harmonic Balance Method

Harmonic Balance Method (HBM) is a good method to find the best approximate harmonic solution of the problem in the steady state with harmonic forcing ([111] [112]). The following assumptions are the basis for the first order harmonic balance formulation:

1. All the system responses are harmonic with the same frequency of the excitation forces;

2. Only the first Fourier component of the non-linear force has a significant participation in the response of the system;

We write the dynamic equilibrium in the horizontal direction for the mass m in Fig. 8.2 in the most general case where it is subject to linear and non-linear forces.

$$m\ddot{v}(t) + c\dot{v}(t) + kv(t) = F_L(t) + F_{NL}(t) \tag{8.9}$$

According to the assumptions (1.) the displacement can be expressed using a harmonic function with the same frequency of the excitation force and a general phase, i.e. $v(t) = v_1^* e^{i\omega_d t}$, where $v_1^* \in \mathbb{C}$ and $Q(t) = F_L(t) = f_{L,1}^* e^{i\omega_d t}$ where the projection on the real axis is the response to cosine loading while the projection on the imaginary axis is the response to sine loading. We can substitute into (8.9) the first harmonic of displacement, linear and non linear force and dropping $e^{i\omega_d t}$ we obtain:

$$-m\omega_d^2 v_1^* + i\omega_d c v_1^* + k v_1^* = f_{L,1}^* + f_{NL,1}^* \tag{8.10}$$

To obtain f_{NL}^* we hypothesize a v_1^*, reconstruct the hysteresis loop using transition angle in ([111], [113]), find the first order Fourier approximation of the non-linear force obtained, and then solve for v_1^*. Iterations are performed using a non-linear solver to obtain the solution which satisfies the dynamic equilibrium (8.10). Further details about the method can be found in [114].

8.4   Results

8.4.1   Frequency Response Function of the mass

To assess the effect of each parameter on the system response, we vary each of them and compute the Frequency Response Function (FRF) looking for the optimal working condition (minimum

displacement amplitude $|v_1^*|$) for such a damper, using the HBM. The static solution $v_{QSTC} = Q_1/k$ is used to make the displacement dimensionless ($\widetilde{v} = |v_1^*|/v_{QSTC}$) and, defining $\Omega_f = \frac{\omega_d}{\sqrt{k/m}}$, we plot in Fig. 8.3 the dimensionless displacement $\widetilde{v}$ of the mass as a function of Ω_f using the following parameters: $k_d/k = 1.5$, $\eta = 0.9, \delta = 90°$, $\zeta = 0.1$, $\beta = [0.2 - 0.6 - 1.5 - 2.5 - 4]$. Increasing the normal load on the damper (i.e. β) the resonance peak of the system shifts from $\Omega_f = 1$ to $\Omega_f \simeq 1.6$. The last is of course approximately the value of $\Omega_f = \sqrt{1 + k_d/k} \simeq 1.58$ which corresponds to the natural frequency of the system when the damper sticks. In the middle, the optimum response of the system is obtained, which minimizes the maximum oscillation amplitude at the resonance frequency. It can be seen that the optimum value of β, for the parameters chosen, is ~ 1 and that the FRF moves in between the free response and the stick response, as in the middle the departure is due to damper stick-slip behavior.
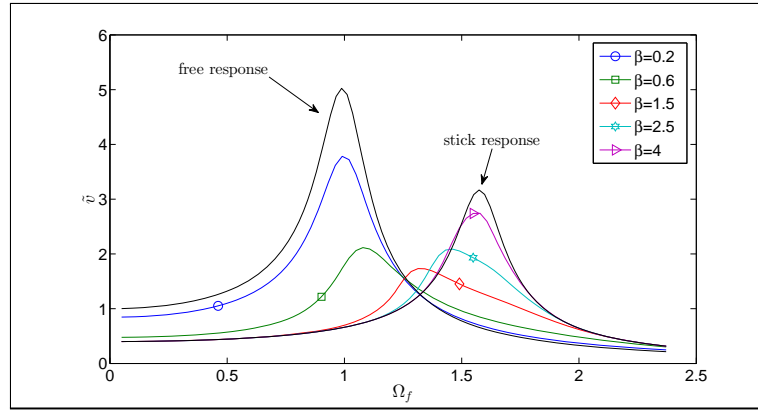
Figure 8.3 FRF for $k_d/k = 1.5$, $\eta = 0.9$, $\zeta = 0.1$, $\beta = [0.2 - 0.6 - 1.5 - 2.5 - 4]$

In Fig. 8.4 (a), the frequency response functions for $k_d/k = 1.5$, $\eta = 0.9, \beta = 1.1$, $\zeta = 0.1$ are plotted for 6 values of phase shift $\delta = [0° - 10° - 30° - 50° - 70° - 90°]$.

Looking at the effect of phase shift δ, moving from in phase loading ($\delta = 0°$) to quadrature loading ($\delta = 90°$) there is a general increment of the displacement amplitude up to the resonance peak that is actually well damped, whereas after the peak all the response collapse towards the stick case, broadly speaking without dependency on the phase shift. Fig. 8.4 (b) shows the ratio between $\widetilde{v}$ and $\widetilde{v}_{\eta=0}$ that is the correspondent response of the system with constant normal load on the damper. It shows that for quadrature loading the displacement increment is around 60% while the decrement after the peak is only of the 10%.
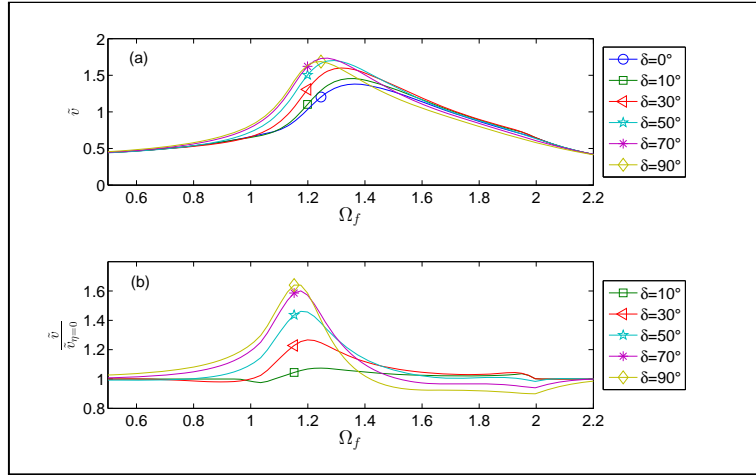
Figure 8.4 FRF for $k_d/k = 1.5$, $\eta = 0.9$, $\zeta = 0.1$, $\beta = 1.1$, $\delta = [0° - 10° - 30° - 50° - 70° - 90°]$

In Fig. 8.5 (a) the vibration amplitude as a function of η is shown, with a focus on the in-phase loading. We choose the following parameters: $k_d/k = 1.5, \beta = 1.1, \zeta = 0.1, \eta = [0-0.3-0.6-0.9]$. Figure 8.5 (b) shows the ratio between the displacement and the correspondent case with constant normal load. It seems that for in-phase loading the parameter η has a little influence on the system response, which causes a variation within $\pm 5\%$. In particular, the increments are evaluated near the peak and decrement on both sides.

More interesting is the effect of η when quadrature loading occurs; Fig. 8.6 (a) reports the FRF for the same parameters used before, but for $\delta = 90°$ and in Fig. 8.6 (b) we plot the ratio $\widetilde{v}/\widetilde{v}_{\eta=0}$. The last figure allows to note that if normal load is varying enough, the increment in vibration can be around 60% in the zone of the system resonance, whereas afterwards a decrement of 15% can be reached. This shows that nearby the optimum β the key parameter is the phase shift δ rather than the magnitude of normal load variation. If in-phase loading occurs, the system response is very marginally affected by normal load variation, while quadrature loading is very detrimental to effectively damp vibrations.
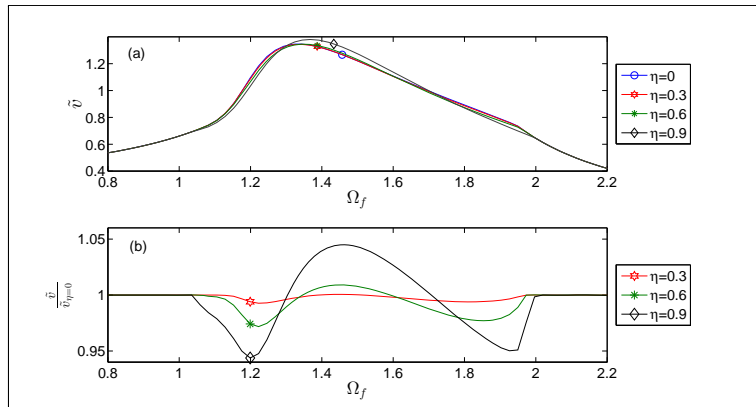
Figure 8.5 FRF for $k_d/k = 1.5$, $\delta = 0°, \beta = 1.1$, $\zeta = 0.1$, $\eta = [0 - 0.3 - 0.6 - 0.9]$
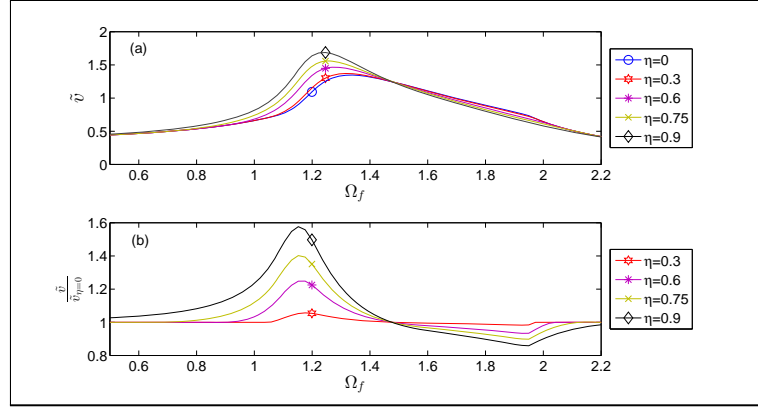
Figure 8.6 FRF for $k_d/k = 1.5$, $\delta = 90°$, $\beta = 1.1$, $\zeta = 0.1$, $\eta = [0 - 0.3 - 0.6 - 0.75 - 0.9]$

So far we showed how the system is affected by the parameters η and δ near the "optimum β", which we further specify here. Increasing β, the system moves from the free to the stick response, reaching a minimum in the middle (see Fig. 8.2). Hence, we drew the optimization curve of the system taking the maximum value of the vibration amplitude (at the resonance) for each β. The result is shown in Fig. 8.7 (a), while for a better comparison in Fig. 8.7 (b) the ratio $\widetilde{v}/\widetilde{v}_{\eta=0}$ is plotted. The curve in blue (triangle marker) shows the case for constant normal load. It is worth saying that such a model for constant normal load was solved by Griffin in closed form [108], which was used as reference to validate our codes. Turning back to Fig. 8.7 (a), the curve in green (asterisk markers) represents the case $\eta = 0.9$ and in-phase loading, while that in red (dot markers) refers to $\eta = 0.9$ and quadrature loading. Looking at the shape of the optimization curve, it is seen that increasing β (i.e. the mean normal load on the damper) the maximum displacement decreases, than reaches a minimum near $\beta \simeq 1$ and then increases again. Of course when β is high enough to bring the damper in the stick condition at all loading frequencies, the peak remains stuck at the same value ($\simeq 3$) for all β.

A closer look to the results obtained shows that for quadrature loading, the vibration amplitude increases near the minimum, with an increment that is around the 25%. If the case of in-phase loading is considered, the curve behaves as in the constant normal load case up to the minimum, but for β higher than $\beta_{opt} = 1$ an important reduction in displacement amplitude is registered. Fig 8.7 (b) shows that the decrement can be larger than 30% for β around 5. This reduction for $\beta > \beta_{opt}$ is of particular interest from an engineering point of view as it is worth to work on the strengthening branch of the curves, which allows a more stable position if little variations of the parameter β occurs. The design of a damper to operate exactly at the minimum in fact is against robustness, as it leads to large increments of displacement if any small reduction of normal load occurs. Above $\beta = 11$, all the curves collapse to the stick system response.
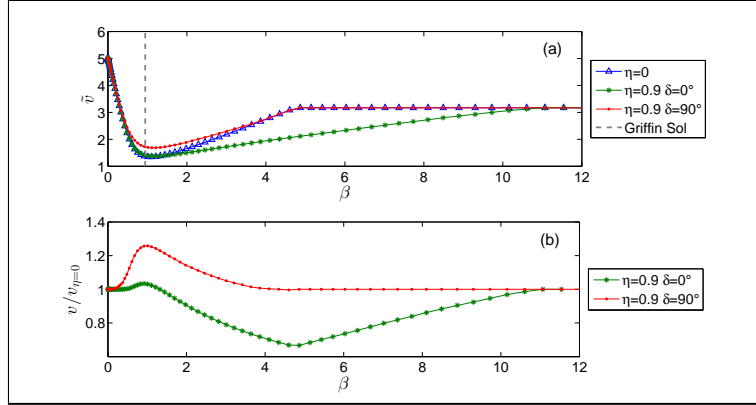
Figure 8.7. (a) Displacement amplitude against β for $k_d/k = 1.5$ (b) $v/v_{\eta=0}$ plotted versus β

We reported in Figure 8.8 (a-b-c-d) the result of the transient simulations for $k_d/k = 1.5, \eta = 0.9, \beta = 5$, $\delta = 0°$ and $90°$, which, as seen in Fig. 8.7, is of particular interest due to the reduction of 30% in the vibration amplitude for the case of in-phase loading. In particular in Fig. 8 (a) and (b) the dimensionless displacement of the mass $v/v_{n=0}$ against the time and in Fig. 8.8 (c) and (d) the phase plots for the damper are shown, respectively on the left side for $\delta = 0°$ and on the right side for $\delta = 90°$. It can be seen that after the transient the mass reaches a steady-state condition with a higher amplitude for the case $\delta = 90°$. This behavior can be clarified looking at the hysteresis loops of the damper (see Fig. 8.8 (c-d)) which show a higher dissipation for the case $\delta = 0°$ than for the case $\delta = 90°$.
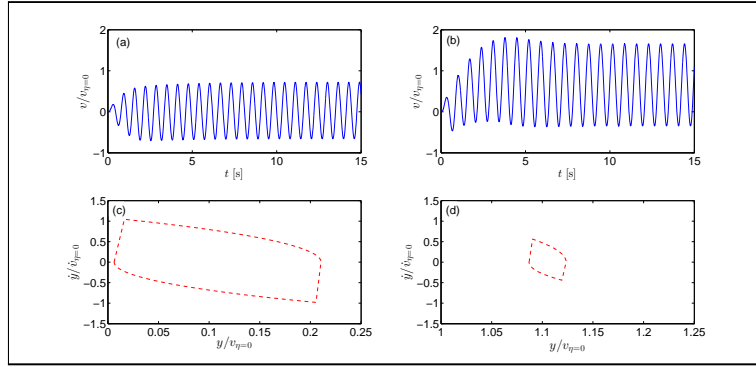
Figure 8.8 (a-b) Dimensionless displacement of the mass $v/v_{n=0}$ against the time for $k_d/k = 1.5, \eta = 0.9, \beta = 5$, $\delta = 0°$ and $\delta = 90°$. (c-d) For the same simulations, phase plot for the damper respectively for $\delta = 0°$ and $\delta = 90°$.

8.4.2 Comparison with quasi-static predictions

It is interesting to compare the prediction of the quasi-static response which is much easier to obtain (it would be even more in large systems), with the full dynamic case. The authors showed in [115] that for a single concentrated mass model, the dynamic solution tends to the quasi-static one in terms of displacement, while this is not true for velocities, because of a possibly large number of intermediate stops. In this case, the response for $\Omega_f = 0.05$ against β is shown in Fig. 8.9, which allows a direct comparison with Fig. 8.7 as the same parameters were used. It is shown that in the quasi-static limit, the displacement amplitude decreases with β and near $\beta = 1$ all the curves approach $\widetilde{v} = 0.4$ which is the static solution when the damper sticks. Afterwards, the

system response starts always from the stick case so no differences occur when increasing β. The β dependence towards the stick quasi-static value is the same for constant normal load and in-phase loading, while the case of quadrature loading is only in qualitative agreement with the dynamic case.

The authors checked the solution on a wide range of k_d/k ratios concluding that the stiffness ratio changes quantitatively the curves due to system strengthening, but qualitatively the behavior results always in an important vibration reduction when the loading is in-phase. To give a closer look to the effect of the stiffness ratio we computed the optimization curves in a range spanning 2 orders of magnitude from $k_d/k = 0.1$ to $k_d/k = 10$, always using $\eta = 0.9$, $\zeta = 0.1$ and working on the two cases of interest: $\delta = 0°$ and $90°$. Note that over all the range for β the ratio $\widetilde{v}/\widetilde{v}_{\eta=0}$ is bigger than 1 for quadrature loading and is almost always lower than 1 for in-phase loading (see Fig. 8.7 (b)). Thus to have a satisfactory summary of the results obtained for different stiffness ratio is sufficient to plot the maximum $\widetilde{v}/\widetilde{v}_{\eta=0}$ for $\delta = 90°$ and the minimum $\widetilde{v}/\widetilde{v}_{\eta=0}$ for in-phase loading.
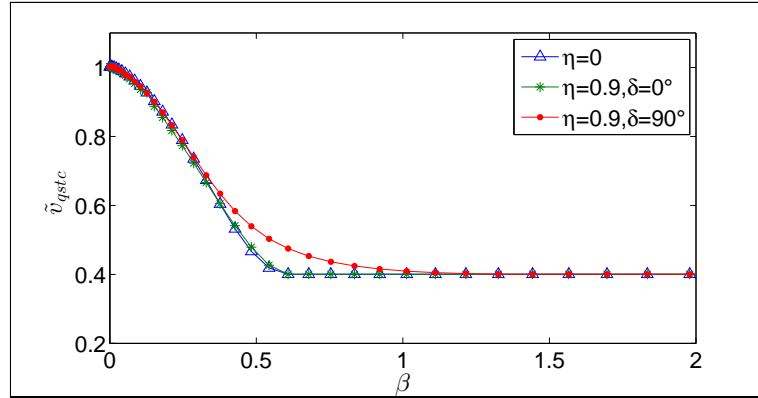
Figure 8.9. Quasi-static displacement as a function of β. Triangle marker for $\eta = 0$, asterisk marker for in-phase loading $\eta = 0.9$, dot marker for quadrature loading $\eta = 0.9$.

Figure 8.10 reports the results obtained: the red solid line (circle markers) refers to the quadrature loading case while the blue solid line (square markers) refers to the case $\delta = 0°$. The curves indicate that for $k_d/k \to 0$ both the ratios $(\widetilde{v}/\widetilde{v}_{\eta=0})_{\text{max/min}}$ go to 1. This is due to the fact that the system tends towards a mass-spring-dashpot without Coulomb damper whose contribution is cancelled out by the vanishing stiffness k_d. When k_d/k is increased, a large increment in displacement amplitude is obtained for quadrature loading that seems to saturate when $k_d/k \to 10$ just over the 40%, while for in-phase loading a decrement of 40% when $k_d/k \to 10$ is shown. A breakthrough for the model is obviously $k_d/k = 1$ as for $k_d/k \ll 1$ the model tends to a viscous damped harmonic oscillator, whereas for $k_d/k \gg 1$ the model tends to the Den Hartog single degree of freedom Coulomb damper ([90]).
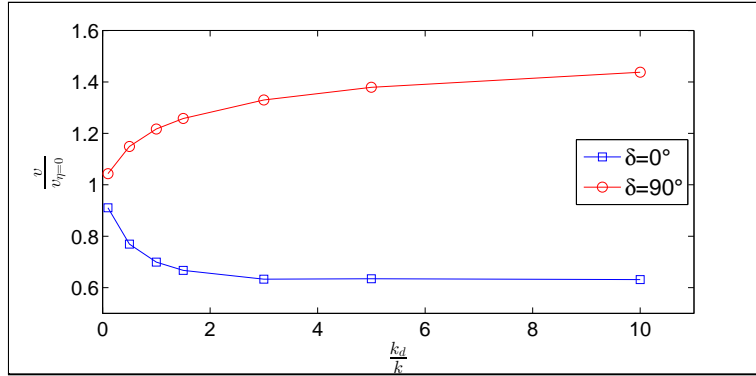
Figure 8.10. The ratio $v/v_{\eta=0}$ is plotted versus the ratio k_d/k. The red solid line (circle markers) refers to $\delta = 90°$ and reports $(v/v_{\eta=0})_{\max}$, the blue solid line (square markers) refers to $\delta = 0°$ and reports $(v/v_{\eta=0})_{\min}$.

8.5   Conclusions

In this chapter we studied a lumped model which is composed of a system mass-spring-dashpot linked by a spring to a Coulomb damper. Our scope was to further clarify the effect that the normal load variation has on the effectiveness damping of vibration with respect to the results of a simpler model [113], which wasn't able to make optimal choice criteria. We show that such a model is a general scheme that could be useful for better understanding of friction dampers used in both civil and mechanical engineering. The minimum of the optimization curve seems to be not affected by the normal load variation and the optimum β still lies where predicted by Griffin in [108] for constant normal load. Nevertheless, in engineering practice the optimum solution (that with the minimum displacement amplitude) should be avoided as it is very close to resonance of the free system. More useful for practical scope is the curve branch with $\beta > \beta_{opt}$ as due to the low slope the system response is not largely affected by a variation of the mean normal load. In this branch, if the loading is varied in-phase, for example coupling it with the tangential vibration of the structure, a reduction of the 30% in vibration amplitude can be achieved. Vice versa, quadrature loading is detrimental near β_{opt} as it leads to increment of vibration amplitude of about 30%: for higher β the response tends to match the case of constant normal load. We conclude that damper designer should prefer to use in-phase normal load variation to more effectively damp the system vibrations.

Chapter 9

A self-excited nonlinear oscillator chain with cyclic symmetry

In the previous chapters we have studied the dynamic of a single mass tangentially loaded, that slides against a frictional plane or is elastically linked to a massless damper. Here we will consider a chain of mechanical nonlinear oscillators, weakly coupled and subjected to self-excitation. The nonlinearity is described via a polynomial force of degree five which incorporates all the nonlinear effects. In some ranges of the parameters governing the problem multiple stable and unstable solution are found which are very similar to the snaking bifurcations, well known in other physics fields.

9.1 Introduction

Spatially localised states of dynamical systems have been studied in a large number of different fields in the sciences and in engineering. While for linear systems Anderson localisation was the key to quite a satisfactory understanding, in nonlinear dynamical systems the quest to understand localisation seems far from settled. For a long time progress seems to have been largely confined to conservative nonlinear systems, where solitons and breathers made their appearance. Only later, dissipative systems have come into focus, with first work based on tracing solitons into the driven and dissipative regime, introducing dissipative solitons. In parallel to the study of solitary states in conservative and dissipative systems, another breakthrough to the understanding of spatial localisation in dissipative localisation was accomplished in the study of subcritical bifurcations in pattern-forming systems, where the concept of branching has emerged and is a well-established field of study today.

Branching is today well known in a number of disciplines, amongst others in optics [116], granular matter [117], structural mechanics ([118], [119], [120], [121], [122], [123]), and mostly in fluid dynamics ([116], [124], [125], [126], [127], [128]), and magnetohydrodynamics ([129], [130]). The first studies into the topic have probably emerged in the field of binary-fluid convection, where spatially localised convection rolls have been observed in water-ethanol mixtures [124] or helium [125]. There localised convection domains of arbitrary length are found to be stable, being surrounded by the conductive state.

In terms of bifurcation diagrams, the localised states have shown to be arranged in a unique and fascinating way, giving birth to what is called a snaking structure ([126], [127], [130], [121]). The snaking structure has e.g. been studied a lot in the one dimensional [131] and the two dimensional [132] Swift-Hohenberg equation, which is a convenient and general model system to study fundamental properties of the arising dynamics.

A typical snaking bifurcation diagram involves two snaking solution branches, intertwined into each other. Figure 9.1 gives an example from convection [127] to illustrate the phenomenon. For the bifurcation diagram (left panel), the average kinetic energy "E" of the flow is plotted versus the Rayleigh number "Ra" and two intertwined branches appear. In the right panel, nineteen solutions are shown, which correspond to the numbers positioned close to the snaking structure, in which spatially localised convective rolls can be identified. Notice that the higher the energy of the solution, the larger the number of convection cells. Often the two snaking branches are also interconnected through a number of unstable branches, and a ladder like pattern emerges [132].

Although snaking bifurcations are now generally known and studied in many fields of dynamical systems, it seems that there is hardly any study into the phenomenon in the context of structural vibrations in engineering. In many respects this is quite surprising, since non-linear oscillators with subcritical Hopf bifurcations, often coupled to neighbouring oscillators of the same type into chains or arrays, are actually very common models for a number of systems from engineering vibrations. And also the appearance of bi- or multi-stability, which is obviously at the core of the phenomenon ([128], [131], [132]), is well established in many of these engineering systems. Moreover, the emergence of spatially localised vibration states in structural dynamics is also a well known observational fact: e.g. in turbo-machinery, there is the so-called effect of 'mis-tuning in rotors' ([133], [134]). Traditionally, the origin of the localisation is thought to have its root in slight system inhomogeneities, leading to linear localisation in the sense of Anderson. From testing, strong localisation is confirmed, but proper validation of the theory has up to now not been accomplished in the linear framework. In a sense it is tempting to hypothesise that one of the key reasons behind might be the non-linearity involved, which definitely becomes substantial for the large local vibration amplitudes observed. To the best of our knowledge, in model systems for turbo-machinery dynamics, snaking behaviour has never been investigated. Also systems from fluid-structure-interaction, may show weak non-linearity, Hopf bifurcation, and bi-stability, like models for aerofoil flap dynamics ([135], [136], [137], [138]). Similarly in friction induced vibrations the emergence of snaking could be well expected, with all the necessary ingredients like flutter instability and bi-stability already known to exist, cf. e.g. ([139], [140]).

We will thus consider a model system as simple as we can think of, but derived from models actually in use in the turbo-machinery community and the field of fluid-structure interaction and friction-induced vibration. We choose a chain of (weakly non-linear) oscillators coupled into a linear oscillator chain. For simplicity we close the chain into a cyclically symmetric ring, which moreover has the advantage of bringing it even closer to models used widely in turbo-machinery for rotors with a small but finite number of blades attached. To obtain or model instability and spatially local bifurcation, i.e. the bi-stability of the individual oscillator, we introduce non-linear damping terms, i.e. non-linear terms depending on velocities. This approach is heuristic and rather for simplicity at the present stage of understanding, but can be thought of bringing into our purely structural model the corresponding non-linear forcing and dissipation terms from surrounding flow, or an involved friction interface.

With a velocity dependent force arising from a fifth order polynomial representation, our system results in individual uncoupled oscillators showing subcritical Hopf bifurcations and bistability, while the oscillator chain, i.e. the coupled oscillators, yield snaking bifurcations that we determine by solving algebraic equations or time-integration. Interestingly, the results do turn out different to many of the hitherto reported snaking bifurcation patterns. The snaking observed in our study seems to show more than a single snake-and-ladders pattern, and much of the pattern as a whole seems to have disintegrated into isolated branches, now usually called isolas. Reviewing where these differences might come from, shows that the key features where our system is different, can easily be identified. First of all, our system is discrete. Individual self-excited oscillators are coupled, as e.g. in the work of Yulin and Champneys in [141], where a one-dimensional periodic array of optical cavities pumped by coherent light were studied. As in our results, the effect of discreteness was studied, showing that the pinning region (the parameter interval where the snaking occurs)

gets progressively narrower as the continuum limit is approached. The second characteristic of our system that is slightly unusual is its finite size due to the cyclic symmetry, which does not allow arbitrary wave-numbers or wavelengths to appear, and so does put a constraint onto the system. Formally similar, Taylor and Dawes in [142], studied snaking and localised states in spatially discrete problems for modified periodic or phase shifted boundary conditions. Also in their case, isola rather than continuous snakes have been observed.
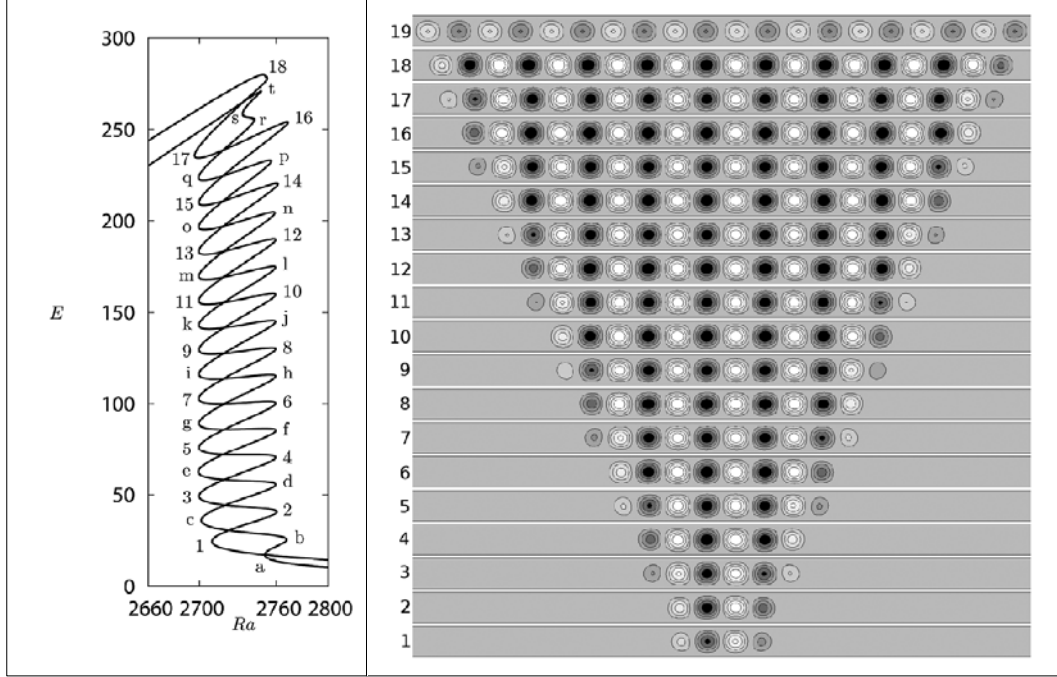
Figure 9.1 An example for snaking in a convection system. Adapted from [127]. Left: typical snaking pattern with two intertwined solution branches in the bifurcation diagram with kinetic energy "E" of the fluid plotted versus the Rayleigh number "Ra" . Right: The stream-functions for solutions as marked in the snaking pattern. The graphs show the spatially localised convection patches.

9.2 The mechanical system

We consider a cyclic system of N_{dof} non-linear oscillators, see Fig 9.2, which are coupled via a weak linear spring of stiffness k_Δ. Each oscillator has mass m and is linked to the ground via a linear spring k and a non-linear damper which introduces a velocity proportional force of the form

$$F_v = -c_1 \dot{x} + c_3 \dot{x}^3 - c_5 \dot{x}^5. \tag{9.1}$$

Here x denotes the displacement of the individual oscillator, $\dot{x}$ the velocity, and we introduced the coefficients c_1, c_3, c_5 to parametrise the velocity-dependent force.
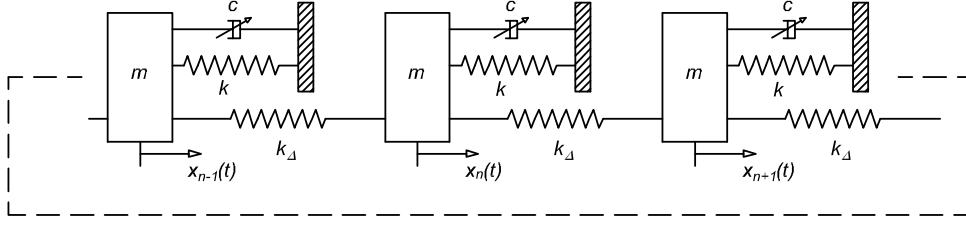
Figure 9.2 The model system under study.

The evolution equations for the individual oscillators read

$$m\ddot{x}_n + c_1\dot{x}_n - c_3\dot{x}_n^3 + c_5\dot{x}_n^5 + kx_n - k_\Delta\left(x_{n+1} + x_{n-1} - 2x_n\right) = 0, \tag{9.2}$$

where the stiffness k_Δ couples the n-th mass with the neighbouring ones. We introduce the quantities $\omega_0 = \sqrt{k/m}, \eta_\Delta = k_\Delta/k, \xi_i = \frac{c_i}{2\sqrt{km}}, \tau = \omega_0 t$, divide the equation (9.2) using the group $\omega_0^2 x_0$, with x_0 a reference displacement, obtaining

$$q_1\ddot{\tilde{x}}_n + q_2\dot{\tilde{x}}_n - q_3\dot{\tilde{x}}_n^3 + q_4\dot{\tilde{x}}_n^5 + q_5\tilde{x}_n - q_6\left(\tilde{x}_{n+1} + \tilde{x}_{n-1} - 2\tilde{x}_n\right) = 0, \tag{9.3}$$

where

$$q_1 = 1, \quad q_2 = 2\xi_1, \quad q_3 = 2\xi_3\omega_0^2 x_0^2, \quad q_4 = 2\xi_5\omega_0^4 x_0^4, \quad q_5 = 1, \quad q_6 = \eta_\Delta, \tag{9.4}$$

and the $\widetilde{\square}$ superposed indicates that the new displacements are dimensionless, $\tilde{x}(\tau) = x(\tau)/x_0$. In (9.3) we defined a dimensionless time $\tau = \omega_0 t$, which allows to replace $\frac{d}{dt}$ with $\omega_0\frac{d}{d\tau}$. Notice that we choose $\xi_3, \xi_5 > 0$, thus the third degree term of the velocity-dependent force introduces a destabilizing force into the system, while the fifth degree term tends to stabilize it. Figure 9.3 (a) lists the arbitrary but characteristic parameters that will be used in the next sections. We will choose ξ_1, i.e. the linear damping coefficient, as our primary control parameter in a range from -0.4 to $+0.6$. In this range the velocity dependent force changes its shape in a way such that for low ξ_1 values a negative damping is introduced, which is often used in the literature to model self-excited vibrations, such as in fluid- or friction-induced flutter [143] or squeal [144].

9.3   Numerical algorithm

9.3.1   Harmonic Balance Method (HBM)

The problem to solve is composed of N_{dof} second order differential equations. In this study periodic vibrations will be considered only. We therefore apply the Harmonic Balance Method (HBM) as an efficient numerical technique to obtain an approximation to the steady-state solution of the system. In the following we briefly recall the main steps of the HBM, further details can e.g. be found in [114]. Consider a time dependent signal $x(t)$ and express it in a Fourier series

$$x(t) = \frac{a_0}{2} + \sum_{h=1}^{N_h}\left(a_h\cos\left(\omega h t\right) + b_h\sin\left(\omega h t\right)\right), \tag{9.5}$$

where ω is the fundamental frequency, N_h is the number of harmonics considered and

$$a_h = \frac{2}{T} \int_{-T/2}^{T/2} x(t) \cos(\omega h t) \, dt, \tag{9.6}$$

$$b_h = \frac{2}{T} \int_{-T/2}^{T/2} x(t) \sin(\omega h t) \, dt. \tag{9.7}$$

A set of non-linear algebraic equations is obtained by substituting the dimensionless form of eq. (9.5) into (9.3) and projecting the equilibrium equations on the Fourier basis $1, \sin(\rho h \tau), \cos(\rho h \tau)$ for $h = 1, ..., N_h$. The projection gives back a system of algebraic equations in which the unknowns are the Fourier coefficients a_h, b_h of the N_{dof} degrees of freedom (dof) considered. In our particular case the dynamical system is autonomous (there is no forcing term) and therefore the angular frequency of the solution ω is also treated as an unknown.

9.3.2   Numerical solution and continuation

The number of algebraic equations to be solved is $(2N_{dof}N_h + 1)$. If only one harmonic is considered ($N_h = 1$) the system of equations for the n-th mass is

$$\begin{cases} \frac{5}{8}q_4\rho^5 \left(a_n^2 + b_n^2\right)^2 b_n - \frac{3}{4}q_3\rho^3 \left(a_n^2 + b_n^2\right) b_n + \rho\left(q_2 b_n - \rho q_1 a_n\right) + \\ \qquad + a_n\left(q_5 + 2q_6\right) - q_6\left(a_{n-1} + a_{n+1}\right) = 0, \\ \frac{5}{8}q_4\rho^5 \left(a_n^2 + b_n^2\right)^2 a_n - \frac{3}{4}q_3\rho^3 \left(a_n^2 + b_n^2\right) a_n + \rho\left(q_2 a_n + \rho q_1 b_n\right) + \\ \qquad - b_n\left(q_5 + 2q_6\right) + q_6\left(b_{n-1} + b_{n+1}\right) = 0, \end{cases} \tag{9.8}$$

where a_n (b_n) is the first harmonic cosine (sine) coefficient. It will be shown later that in most parameter ranges even with just one harmonic the approximate solution is very close to the exact one, therefore we will mostly use one harmonic only, which leads to a system of $2N_{dof}$ polynomial equations of the fifth order. The other equation comes from the projection of the equilibrium equation on 1, which would allow for evaluation of the mean displacement over a period. As the non-linearities are odd and there is no constant term in the equations, the mean displacement always vanishes. The system of $2N_{dof}$ polynomial equations has been solved using a Newton-Raphson scheme implemented in the MATLAB$^{\circledR}$ function *fsolve*. For a fixed value of ξ_1, a set of initial conditions has been provided using steady state solutions obtained from a time integration algorithm. Localised as well as non localised solutions were used as a starting point for the Newton-Raphson algorithm. To solve the system we set for one mass $b_1 = 0$, which allows us to solve for the fundamental frequency of the solution too. A continuation algorithm, also implemented in MATLAB$^{\circledR}$, continued the solution using a pseudo arc-length scheme [145] which allowed to follow the solution trajectory even when turning points were encountered [145].

9.4   Simulation Results

9.4.1   Single oscillator dynamics

Here we concentrate our attention on the behaviour of a single oscillator when it is isolated from the rest of the chain. The following parameters will be used:

$$\omega_0 = 2\pi, \quad x_0 = 1, \quad \xi_3 = 0.3, \quad \xi_5 = 0.1, \quad \eta_\Delta = 0. \tag{9.9}$$

In Figure 9.3 (b) we plot the maximum potential energy of the mass in dimensionless form: $\widetilde{U}_{\max} = \frac{1}{2}\widetilde{x}_{\max}^2$, where $\widetilde{x}_{\max}$ is the vibration amplitude at the steady-state condition. The results have been obtained using three different approaches: circles represent the result of the Time Integration (TI), the solid line shows the result obtained using the HBM where $x(t)$ is approximated with only the

first harmonic, while the dashed line is the result obtained using the HBM with two harmonics, the first and the third. The choice of the first and third harmonics takes into account the fact that the non-linearities introduced are odd and symmetry breaking bifurcations are not considered in this work. We start focusing on the TI results (circles). When $\xi_1 \gtrsim 0.2$ only one solution exists in which for every initial condition the vibration is damped and vanishes. Decreasing ξ_1, in the range $0 < \xi_1 \lesssim 0.2$ another solution appears with $\widetilde{U}_{\max} > 0$ which corresponds to a stable limit cycle of finite amplitude. The single oscillator experiences a subcritical Hopf bifurcation, and in the interval $0 < \xi_1 \lesssim 0.2$ two different stable solutions exist. Notice that using TI, only the stable solutions can be found (Figure 9.3 (b) circles), while HBM also allows to obtain the unstable ones and to follow them. If $\xi_1 < 0$ the steady state is not stable and the vibration amplitude grows up to the upper branch with $\widetilde{U}_{\max} > 0$. In this range the only stable solution is a limit cycle for which the amplitude grows when ξ_1 is further reduced. Figure 9.3 (b) also shows the results obtained using HBM with one harmonic (solid line) and with two harmonics (dashed line). First we note that in the interval $0 < \xi_1 \lesssim 0.2$ another solution appears which represents an unstable limit cycle. Differences in the two curves obtained with HBM appear for the upper branch when ξ_1 decreases, as higher vibration amplitude implies higher contribution of the non-linearities. The solution which includes two odd harmonics approximates very well the exact solution obtained with TI scheme. Nevertheless if we just focus on the interval $0 < \xi_1 \lesssim 0.2$ we can see that even the single harmonic approximation is never too far from the exact solution[1]. In the following sections the oscillator chain dynamics is studied in the bistability zone ($0 < \xi_1 \lesssim 0.2$), and all the results presented will be obtained using HBM with one harmonic.
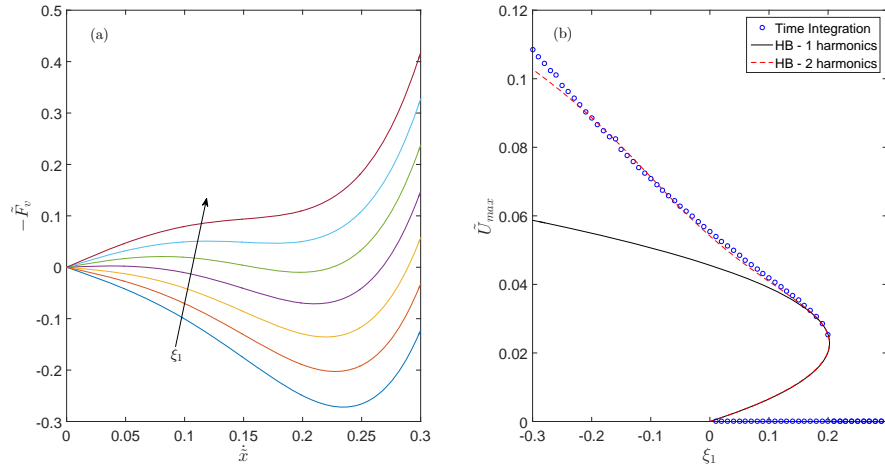
Figure 9.3 (a) Dimensionless velocity dependent force plotted versus the velocity for $\xi_1 = [-0.4, -0.25, -0.1, ..., 0.6]$, $\xi_3 = 0.3$, $\xi_5 = 0.1$, $\omega_0 = 2\pi$, $x_0 = 1$. (b) Maximum potential energy of one single oscillator plotted against the bifurcation parameter ξ_1. Blue dots: results of the time integration at the steady state. Solid line: HB solutions with a single harmonic. Dashed line: HB solutions with two odd harmonics.

---

[1] Also in Figure 8 (left panel) we will plot in the bifurcation diagram TI solutions superposed to the HB solutions to demonstrate that the first order truncation is able to capture the basic features of the exact solution. We are aware that this approximation can smooth out some fine details of the true solution, but the aim here is to focus on the overall result.

9.4.2   Oscillator chain dynamics: linear system

Before studying the dynamical behaviour of a cyclically symmetric chain of $N_{dof} = 12$ non-linear oscillators we analyse the response of the underlying undamped linear system with a dimensionless coupling stiffness $\eta_\Delta = 0.01$. Due to the cyclic symmetry this system presents mostly pairwise degenerate eigenfrequencies that can be computed as [146]

$$\omega_p = 1 + 2\eta_\Delta \left(1 - \cos \left(\frac{2p\pi}{N_{dof}} \right) \right), \tag{9.10}$$

where $p\epsilon\mathbb{N}$ and $0 \leq p \leq N_{dof}/2$ for even N_{dof} or $0 \leq p \leq (N_{dof} - 1)/2$ for odd N_{dof}. Due to the weak coupling among the oscillators the natural frequencies will lie on a narrow band. A possible set of orthogonal normal modes is [146]

$$\phi_0 = [1, 1, ..., 1]^T, \tag{9.11}$$

$$\phi_p^c = [\cos(\theta_p), \cos(2\theta_p), ..., \cos(N_{dof}\theta_p)]^T, \tag{9.12}$$

$$\phi_p^s = [\sin(\theta_p), \sin(2\theta_p), ..., \sin(N_{dof}\theta_p)]^T. \tag{9.13}$$

The following table lists the natural frequencies [rad/s] and Fig. 9.4 shows the normal mode shapes of the undamped linear system.

$$\omega_0 = 1, \qquad \omega_1 = 1.001, \quad \omega_2 = 1.005, \quad \omega_3 = 1.010,$$
$$\omega_4 = 1.015, \quad \omega_5 = 1.019, \quad \omega_6 = 1.020$$
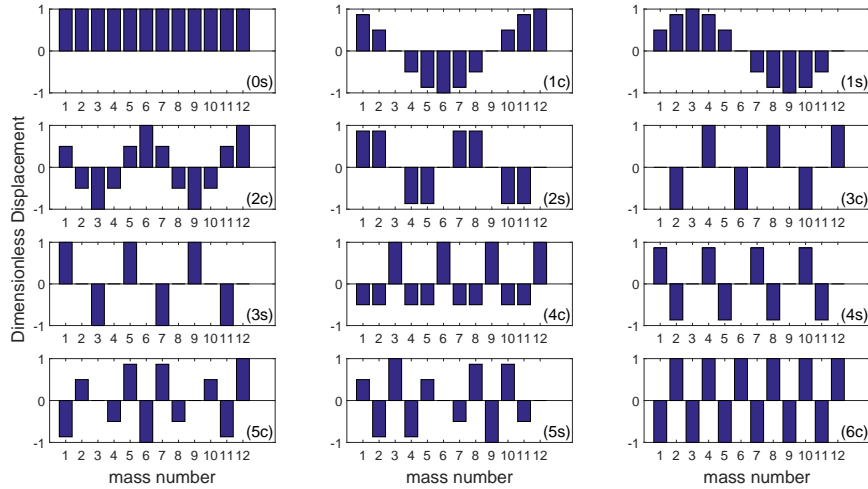
Figure 9.4 Mode shapes of the underlying linear system.

9.4.3   Oscillator chain dynamics: non-linear system

We now study a cyclically symmetric chain of $N_{dof} = 12$ non-linear oscillators in the bistability zone. The parameters used are the same we used for the single oscillators above, except for $\eta_\Delta = 0.01$, which introduces a small coupling between the oscillators. The results obtained from time integration were used to derive initial conditions for the continuation algorithm. Figure 9.5 shows, in the left panel, the sum of the maximum potential energy of each mass $\widetilde{U}_{\max} =$

$\frac{1}{2} \sum_{i=1}^{N} \widetilde{x}_{\max,i}^2 = \frac{1}{2} \sum_{i=1}^{N} \left(\widetilde{a}_i^2 + \widetilde{b}_i^2 \right)$ plotted against the linear damping coefficient ξ_1. Many solutions appear to be entangled, making it almost impossible to distinguish one from the other. Looking more closely at the overall structure created by the superposed solutions we can observe trajectories similar to snake and ladder branches ([126], [127], [121], [130]) and twelve 'steps' (corresponding to the number of oscillators) can be identified. Each step is labelled with a red circle and the corresponding energy distribution is plotted in the twelve bar plots on the right-hand side of Figure 9.5. In each bar plot the mass number has been reported on the x-axis, while the bar height is computed as

$$\widetilde{u}_i = \frac{\widetilde{x}_{\max,i}^2}{\max \left(\widetilde{x}_{\max,i}^2 \right)_{i=1,..,12}}, \qquad (9.14)$$

such that the energy of each oscillator is normalized with respect to the one which is vibrating with the largest amplitude.
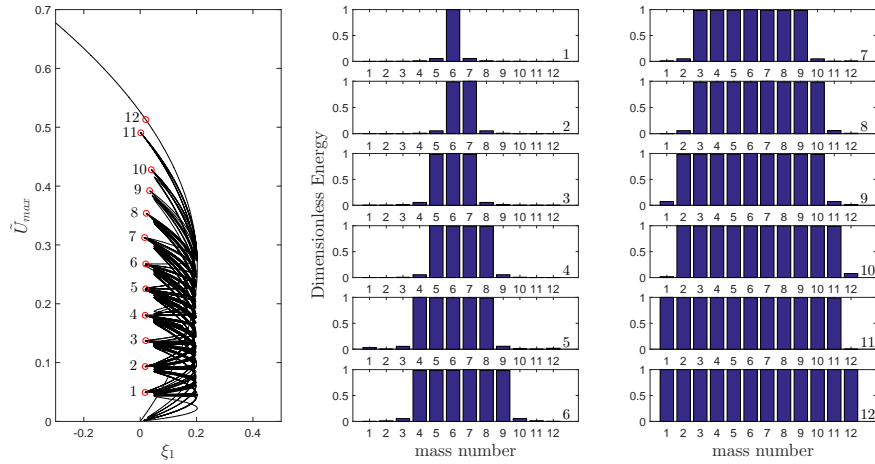
Figure 9.5 Left: bifurcation diagram for the non-linear oscillator chain. The subcritical Hopf bifurcation of the individual oscillator is indicated, and the complex snaking pattern linking the spatially homogeneous stationary static state with the state where all oscillators are vibrating fills the zone of bistability. Middle and Right: the average dimensionless energy of each mass for the 12 equilibrium solutions which are marked with a red circle in the snaking pattern.
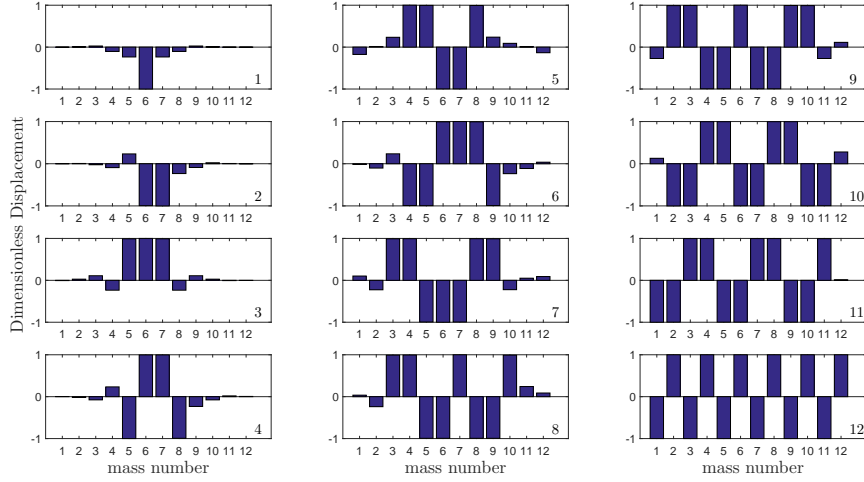
Figure 9.6 In each subplot from 1 to 12 the vibration shape, i.e. with the corresponding phase information, of the solutions in Fig. 9.5 (left panel, red circles) is shown.

The bar plots $1-12$ in Fig. 9.5 shed some light on the system dynamics: each step can be easily related to the number of masses on which the vibration is localised. From the bottom to the top, at the first step one mass is moving while the others are more or less motionless, at the second step two masses are moving and so on up to the twelfth. This resembles the usual snaking behaviour, where, for example in fluid dynamics, the steps can be related to the increasing number of convection rolls. Especially in the bottom part of our snaking (Fig. 9.5, left panel) it is possible to see very close similarities with the classical snaking picture. On the other hand, when increasing the energy, and thus the influence of the non-linearities, the picture gets more and more distorted and only seems to be bounded by the very last branch in which all the masses are moving.

Consequently one might conjecture that the relative phases between the individual oscillators play a special role in our system. Figure 9.6 thus shows the vibration mode shape, indicating the relative phasing between the oscillators, in 12 bar plots numbered from 1 to 12, each-one related to one of the red circles in the bifurcation diagram (Fig. 9.5, left panel). It seems that there is an additional sub-structure due to relative in- or out-of-phase behaviour within our localised vibration zones. Sometimes an oscillator is out of phase with both of its neighbours, sometimes two adjacent oscillators go in phase, but out of phase to their respective other neighbours. At the present state of our study, we have not yet succeeded to obtain a deeper understanding of this result, but think it is at the very heart of the multiplicity of solutions observed. Further studies will need to follow.

At this point it also seems useful to have another look at the numerical accuracy of our computational approach. Figure 9.7 shows in each column results obtained from TI for four solutions using $\xi_1 = 0.1$ and different initial conditions. In particular from the left to the right the vibration is localised on one mass, five masses, eight masses and on all the twelve masses. In the first row the displacement time history is shown at the steady-state, in the second row the solution is shown in the phase space and in the third row the dimensionless maximum potential energy of each mass is given (TI results, dark blue). To assess the effect of the first harmonic truncation on the energy distribution among the different oscillators, HBM results are computed for the same parameter sets and using the TI solutions as starting point. The maximum potential energy, shown in Fig. 9.7 (HBM results, pale yellow bars), proves that the energy is distributed exactly in the same manner and that the low-order approximation causes only a very small reduction in the potential energy of each mass (due to the loss of solution details) which seems acceptable for our purposes. Notice

also that the shape of the solution with all the masses vibrating corresponds very well to the last mode of the linearised system, in which the motion is out-of-phase.
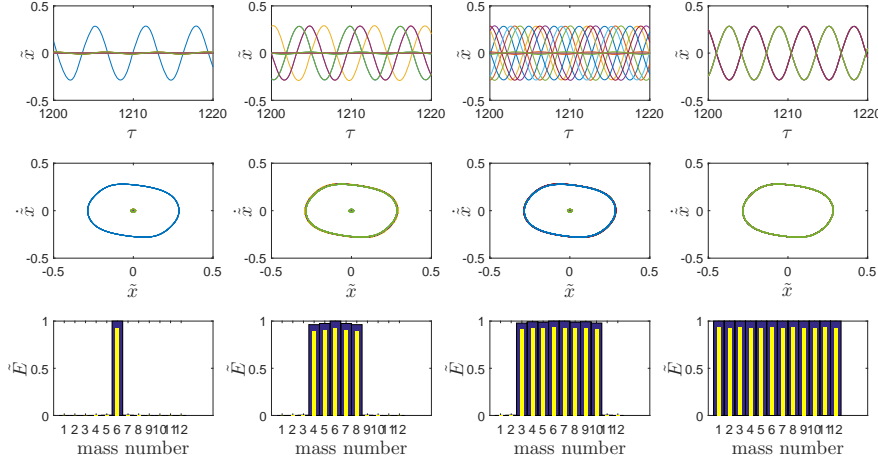
Figure 9.7 Each one of the four columns corresponds to one solution obtained with TI. In the first row the displacement time history, in the second row the space state trajectories ($\dot{\tilde{x}}$ vs $\tilde{x}$), in the third row the dimensionless maximum potential energy of each mass in steady state condition is shown (dark blue). In the third row, the energy distribution obtained with single harmonic HBM is plotted (pale yellow).

9.4.4 Isolas: closed solution branches

Figure 9.5 has suggested that our snaking picture in the bistability zone is more complex than the usual one. In Fig 9.8 (left panel) the snaking picture observed before is thus plotted again, but this time the ensemble of all the solutions is drawn in the background in pale gray, while four branches of solutions are highlighted using thick lines. It turns out that they have a well defined shape resembling a figure eight. Hereafter we will refer to these branches as isolas, since they are isolated. Despite the whole picture seems really intricate, it is made up of a number of such isolas. Closer study shows that our isolas are actually not strictly speaking isolated in the sense that there are no other solutions branching off, but that there are further bifurcations and interlinking solutions and connecting branches involved. We will come back to this point below.

In obtaining the snaking picture we found and plotted 53 isolas and connecting branches. Following the branches of the isolas, localised solutions with a different number of vibrating masses are linked together, which is conceptually linked to the snaking phenomenon. In Figure 9.8 four isolas are selected with the peculiarity to have all the masses moving in out-of-phase manner. On the left panel eight points, lying on the straight line $\xi_1 = 0.15$, are marked with a red circle. The dimensionless vibration shape of each point is graphed in the correspondent bar plot on the right side. Focusing on the pair of points that belongs to the same isola, we can see that increasing the energy of the vibration leads to a higher number of masses involved: for example the first isola links solutions localised on one and three masses vibrating, the second isola links solutions localised on three and five masses vibrating, and so on. Compare the points $2-3$ or $6-7$: they belong to different isolas, nevertheless they are close in the bifurcation diagram. It can be seen that in fact those points have a slightly different vibration shape. Notice that the points 4 and 5

deserve some further attention: both of them involve five vibrating masses, but the solution has a different vibration shape (compare the bar plots of Figure 9.8). These considerations indicate how complicated the snaking phenomenon for our vibration system is, as not only the number of vibrating masses matters, but also the relative phases, i.e. the vibration shape plays a fundamental role.

Again, and just to double-check, in the bifurcation diagram (Figure 9.8, left panel) points obtained via time integration are denoted as red stars to show which branch of the isola is stable. Discrepancies between TI and HBM results are apparent and due to the one harmonic approximation, but small.
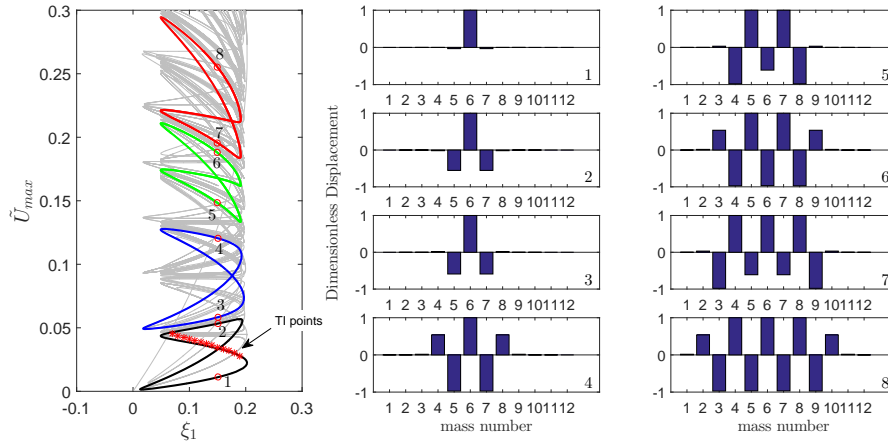
Figure 9.8 Left: The overall snaking pattern is kept in the background, while four isolas are highlighted. On each isola two points are marked with a red circle and a number. Stars indicate time integration results. Right: eight bar plots visualise the shape of the vibration for the corresponding solution marked.

9.4.5   Isolas and connecting branches superposition

We study in some more detail the bifurcation structures of the isolas found. In Figure 9.9 the left panel shows on the background the snaking picture (pale gray), while six solutions are emphasised to show on which part of the pattern they lie. We chose isolas in the bottom part of the pattern because they are less distorted than those in the upper part, and the picture is thus easier to explain. Nevertheless any other choice of the isolas would show the same main features. The six solutions are drawn in pairs, using a solid and a dashed line, into the subplots (a), (b), (c) to show to the reader how they are linked together. Looking at the subplot (a) one can see that the left hairpin bends of the isolas are connected through an independent branch which bifurcates from the isola. The same behaviour can be observed in Figure 9.9 (b) where the branch drawn with the dashed line bifurcates from the isola drawn with the solid line. Figure 9.9 (c) shows two solutions which are very close to each other along one branch. All these six solutions are then superposed to each other in Figure 9.9 (d) to show how the complex overall snaking pattern emerges. Looking at the six solutions as a whole, it can be clearly seen that the snaking branches appear and even the peculiar structure of the 'ladder' (in the sense that they connect two different points of the same isola) is there, indicated by arrows in Figure 9.9 (d).

In sum it almost seems that the usual snaking picture to be found in more strongly non-linear, and perhaps more strongly dissipative systems, is kind of broken into smaller elements, i.e. isolas and connecting branches. Further work on clarifying these aspects is necessary.
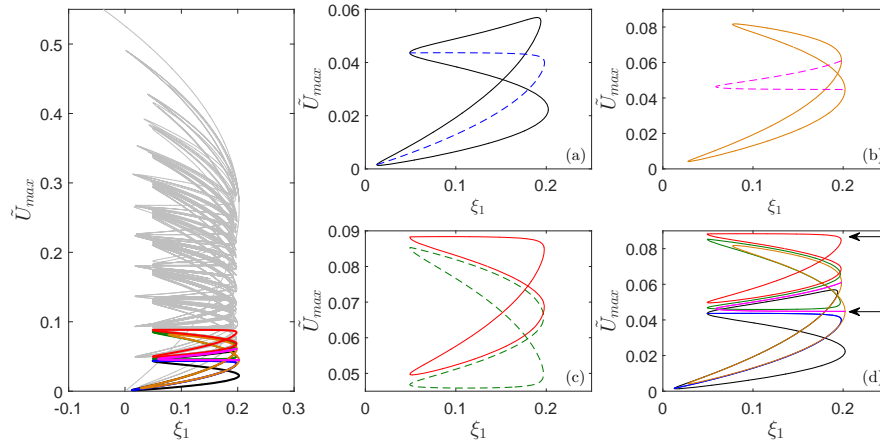
Figure 9.9 Left: Bifurcation diagram in the plane $\left(\widetilde{U}_{\max}, \xi_1\right)$. The snaking structure is left in the background, while six families of solutions are highlighted (thick line). On the right-hand side the six solutions are plotted in pairs (using one dashed and one solid line) into the subplots (a),(b),(c). In the subplot (d) all the six solutions are plotted together to show how they arrange in the overall snaking structure.

9.4.6   Vibration shapes for different solution branches

Here an analysis of the vibration shapes is carried out to show how the solution branches shown in Figure 9.9 relate to different vibration shapes. In Figure 9.10 we plot in the left panel the solution branches again (from Figure 9.9 (a)) in the plane $\left(\widetilde{U}_{\max}, \xi_1\right)$. On the isola of solutions (Figure 9.10) eight points labeled from 1 to 8 are marked with a red circle. We note that the points 8-1-2-3 belong to a part of the isola on which the vibration remains mostly localised on one single mass. After the solution number 3 a hairpin curve brings us to another part of the isola on which the solutions 4-5 show a vibration localised on three masses which vibrate in an out-of-phase manner. Then, for the solutions 6 and 7 the vibration of two of the masses reduces again and the vibration comes back to be localised one on just one mass. We look now at the thick branch of solutions (Figure 10 left panel) which connects two points of the same isola (thin solid line). The solution 11 shows a vibration localised on one mass in a similar manner as for the solutions 7 and 8 on the previous isola. Moving towards the solutions 12-13-...-18 the neighbouring mass starts vibrating in phase with the previous one and the vibration remains localised on two masses (Figure 10) up to the intersection between the connecting branch and the isola. To sum up: while the isola comprises solutions localised on one or three masses, the connecting branch corresponds to solutions localised on one or two masses.
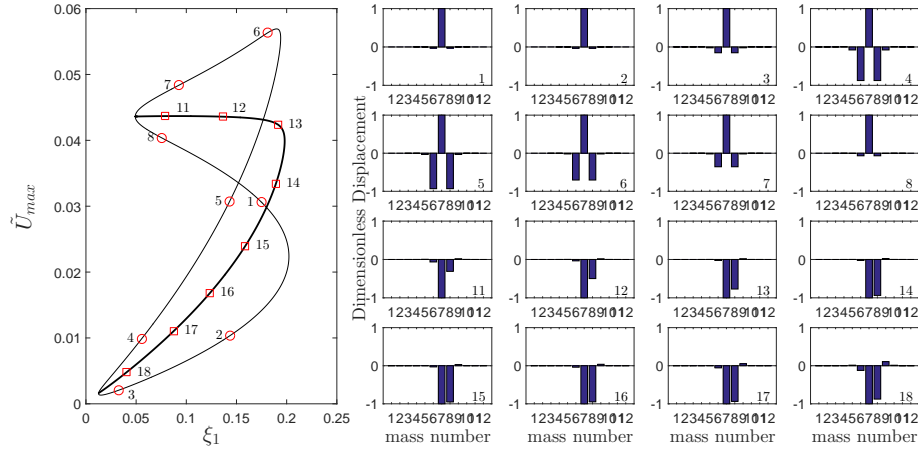
Figure 9.10 Left: two solution branches, or isolas, are drawn (Figure 9.9 (a)) in the plane $\left(\widetilde{U}_{\mathrm{max}}, \xi_1\right)$. On each branch eight points are marked and labelled. For each point the corresponding bar-plot shows the shape of the vibration.

Figure 9.11 shows in the left panel the branches presented in Figure 9.9 (c). In this case the two patterns have both a figure eight shape and they approach each other in the middle zone. The subplots on the right-hand side of Figure 9.11 give the shape of the vibration, while in Fig. 12 the dimensionless energy of each mass $\widetilde{u}_i$ is plotted for the points marked with squares/circles in Fig. 9.11 (left panel). The isola of solutions drawn with a thin solid line connects solutions localised on two masses with others localised on three masses (Fig. 9.11 - Fig. 9.12). The thick solid line isola, instead, links solutions with three vibrating masses with others with four vibrating masses. Moving to the top of the isola, a smooth transition happens from one kind of localisation to the other. It is interesting to compare the solutions 4-5-6-7 with the solutions 18-11-12-13. The two branches are very close together but are not coincident. The solutions (18-4) (11-5) (12-6) (13-7) have the same number of masses involved in the vibration, but with a different shape. Figure 9.12 shows that even if the overall energy of the solutions (in pairs) is broadly the same, it is just distributed differently among the masses due to the different shape. For example if in the subplot 18 of Fig. 9.12 the mass 7 is exchanged with the mass 8 the same distribution that appears in the subplot 4 is obtained, and the same reasoning can be done for the other three pairs, and so on for the whole two branches of the two isolas. Note that this is a feature that enriches the general picture of the snaking phenomena in vibrating systems as the appearance of the many different branches could be thought of to arise from some symmetries in the system. This could explain even why in the upper part of our snaking structure (Fig. 9.5 left panel) the solutions appear more entangled: the larger the number of the masses involved in the vibration, the larger the possibilities to arrange them in different ways.
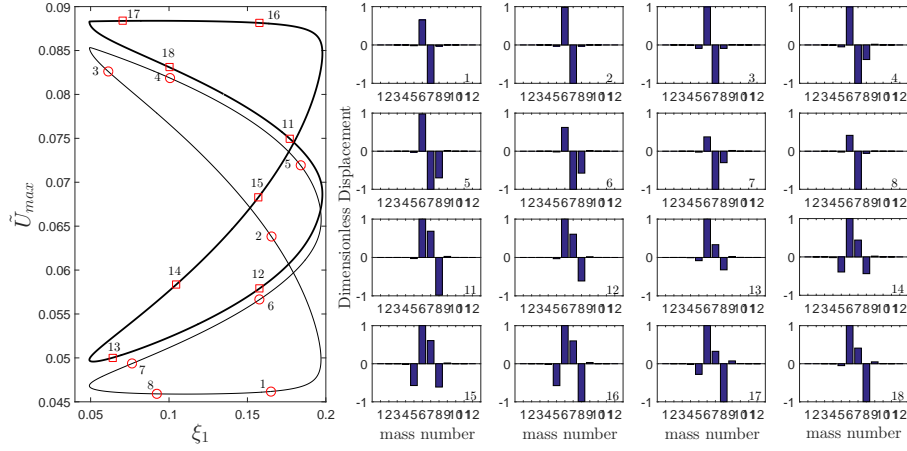
Figure 9.11 Left: two solution branches (Figure 9.9 (c)) in the plane $\left(\widetilde{U}_{\max}, \xi_1\right)$. On each trajectory eight points are marked and labelled with a number. For each number the corresponding bar plot shows the shape of the vibration.
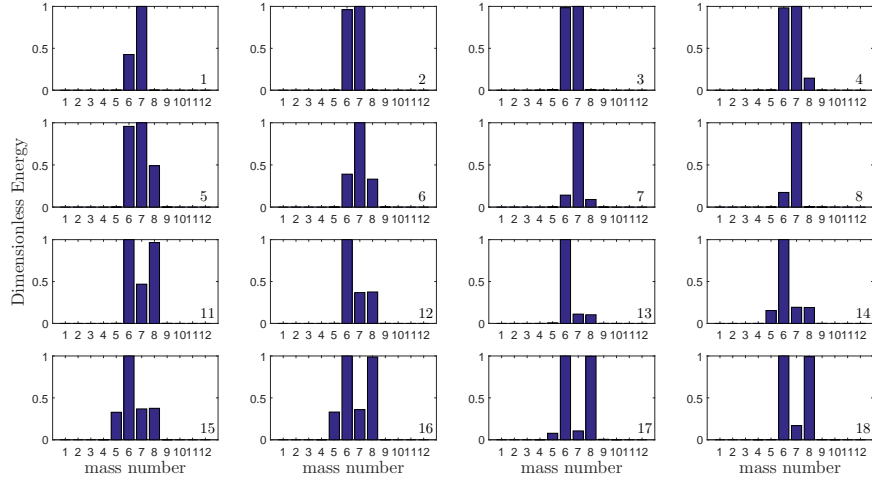
Figure 9.12 Dimensionless energy plotted for each solution marked with the corresponding number from Figure 11.

9.5   Conclusions

In this work we have studied snaking bifurcations of a non-linear cyclically symmetric oscillator chain. Bistability has been introduced in a heuristic manner through non-linear velocity dependent forces. Solutions have been obtained by time integration and harmonic balance techniques. The bifurcation diagrams resulting in the bistability zone resemble typical snaking patterns, but also show marked differences. The solution branches are composed of isolas, which have a figure eight

shape in the bifurcation diagram. When the isolas are put together, they picture a typical snaking pattern, which has been observed in many other fields of physics. Still, our findings suggest that the snaking behaviour in structural dynamics could be more complicated due to the superposition of different non-linear mode shapes: solutions which have very different shapes present almost the same energy content and thus the corresponding solution branches overlap or are very close to each other in the bifurcation pattern.

Physically the snaking phenomenon is due to the weak nearest neighbor coupling among the oscillators and to the positive linear damping coefficient ($\xi_1 > 0$) which damps the small oscillations. In fact when one or few masses are in the high amplitude limit cycle the neighbors can be still stable under small oscillations and don't necessary jump on the high energy solution (limit cycle). We obtain therefore a multitude of solutions (from which, the snaking behavior) because of this bistability between low and high amplitude limit cycles.

From the present results it has become clear that more work on snaking in engineering structures is necessary. Future work will need to focus both on conceptual aspects, as well as on evaluating engineering relevance and impact. As for conceptual understanding, more work is necessary on understanding analogies and differences between the systems under study here and elsewhere. The larger number of states found in the present work needs to be clarified, and the relevance of symmetries, symmetry breaking and imperfect bifurcations, as observed here, needs to be understood better. As for engineering relevance, probably first another set of simplified and idealised model systems, ideally extracted from fluid-structure-interaction, friction-induced vibration, or similar fields, will need to be studied. Thereafter more realistic models, e.g. derived from larger scale computer assisted modelling systems (like finite element analysis or computational fluid mechanics) could be studied.

As for our personal impression about future impact, a deeper understanding of snaking phenomena in engineering systems could make engineers able to better and quantitatively more accurately predict localised non-linear vibration states, which are known to be a source of numerous issues in engineering and technology, like fatigue, strength, or noise. For these reasons we hope that this work might serve as a starting point to conduct further studies on localisation phenomena and snaking in vibration engineering.

Conclusions and outlook

Here the key results of this thesis are summarized to provide to the reader an overall picture of the conclusion that can be drawn from the present manuscript.

In the first part of the thesis the transition between stick and slip has been investigated taking inspiration from some outcomes from the Fineberg's group experiments on the inception of sliding. We have shown that the linear scaling relation between the length of the precursor fronts and the tangential load in Finebger experiments is due to the peculiar geometry used in the experiments and can't be found using halfplane elasticity. Another evidence of those experiments was that close to the interface a local static friction coefficient much higher than the global one, was measured. We proposed a possible explanation that is simply related to the possibility of using a slip weakening friction law at the interface in place of the common and oversimplified Coulomb friction coefficient. Using a double Cattaneo-Mindlin approximation we have shown that when the transition from the static to the dynamic friction coefficient is rapid this model leads to a fracture mechanics field of shear tractions and the inception of slip is controlled via an energetic criterion, a "Griffith friction model". Finally the global static friction coefficient is found when the load-control experiment becomes unstable and overall sliding occurs. Thus, the apparent friction coefficient depends on geometrical effects and external loading configurations, as observed in Fineberg's experiments.

In the second part of the thesis the cyclic response of systems experiencing friction has been studied. First the dynamical behavior of a single degree of freedom with constant normal load and tangentially harmonically loaded was analyzed showing that the dynamic solution for low excitation frequency doesn't converge (for the velocity) to the quasi static solution obtained neglecting the mass terms into the equations. In the bounded regime, if the normal load varies harmonically, the vibration is damped more effectively if normal and tangential loads vary in-phase. We obtained the same conclusion when a more appropriate model was used with a lumped structure linked to a massless damper.

In the last chapter a chain of nonlinear oscillators has been studied inspired to classical models used in turbomachinery. We have shown that in such a system multiple stable equilibrium states exist leading to a bifurcation pattern which is well known in other physics fields, named "snaking bifurcations". It is surprising that such a pattern is, to the best of author knowledge, almost unknown in the mechanical vibration community, although it has been shown elsewhere ([135], [136], [137], [138], [139], [140]) that mechanical systems have all the ingredients (i.e. bi- or multistability) to experience snaking bifurcation as well. In particular, Hoffmann [147] studied a mechanical friction-excited two degrees of freedom system showing that it can experience subcritical Hopf bifurcation (bistability) when, at the contact, the Coulomb friction model with two friction coefficients ($f_s > f_d$) is used. Moreover, if the static friction coefficient is assumed equal to the kinetic $f_s = f_d$ the bifurcation becomes supercritical and the bistability disappears. There is a plenty of literature where friction and nonlinear oscillations are addressed, but in the most of the cases when friction is treated the dynamical properties of the bodies are neglected (Quasi-Static approximation) viceversa when the focus is on the dynamical behavior of systems friction is highly simplified (e.g. Coulomb friction with only one friction coefficient). A natural developments of the work presented in those pages would be to use the knowledge gained into the stick-slip transition

to solve dynamical problems, as different phenomena can emerge that with simpler friction models don't occur.

Appendix A

In this appendix we will solve the partial slip problem presented in chapter 3 (square ended flat punch loaded above the interface line, see Fig. 3.1) using the Griffith friction model presented in chapter 5. All the derivation up to equation (3.17) remains the same except that the condition $q^*(-b) = 0$ translates into a condition on the strength of the singularity (see chapter 5 for the details on the "Griffith friction"), mathematically

$$K_{II} = \lim_{x \to -b^+} q^*(x)\sqrt{2\pi(b+x)} = \tag{A.1}$$

$$= \left[\frac{Q}{2\alpha\pi}\left(\frac{b}{a}+1\right) + \frac{Q-fP}{\pi}\right]\sqrt{\frac{2\pi}{a+b}} \tag{A.2}$$

where $q^*(x)$ is reported in eq. (3.18). Using (A.2) in (3.18)

$$q^*(x) = -\frac{Q}{\alpha a\pi}\sqrt{\frac{b+x}{a-x}} + K_{II}\sqrt{\frac{a+b}{2\pi(x+b)(a-x)}} \tag{9.15}$$

Using a tilde to indicate dimensionless parameter $\widetilde{x} = x/a$, $\widetilde{b} = b/a$, $\widetilde{Q} = Q/fP$, $\widetilde{W} = \frac{\sqrt{E^*W\pi a}}{fP}$, $\widetilde{q}(x) = \frac{q(x)}{fP/(\pi a)}$ and the relation $K_{II} = \sqrt{2E^*W}$ we obtain the dimensionless shear traction distribution

$$\widetilde{q}(\widetilde{x}) = \begin{cases} \frac{\alpha+\widetilde{Q}\widetilde{x}}{\alpha\sqrt{1-\widetilde{x}^2}} & -1 < \widetilde{x} < -\widetilde{b} \\ \frac{\alpha+\widetilde{Q}\widetilde{x}}{\alpha\sqrt{1-\widetilde{x}^2}} - \frac{\widetilde{Q}}{\alpha}\sqrt{\frac{\widetilde{b}+\widetilde{x}}{1-\widetilde{x}}} + \widetilde{W}\sqrt{\frac{(1+\widetilde{b})}{(\widetilde{x}+\widetilde{b})(1-\widetilde{x})}} & -\widetilde{b} < \widetilde{x} < 1 \end{cases} \tag{A.4}$$

From equation A.2 the length of the precursor slip front $\widetilde{l}_{slip} = 1 - \widetilde{b}$ is evaluated

$$\widetilde{l}_{slip} = 2\left[1 - \alpha\left(\frac{1}{\widetilde{Q}}-1\right) - \left(\frac{\alpha\widetilde{W}}{\widetilde{Q}}\right)^2\left(1 + \sqrt{1 - \frac{2}{\alpha}\left(\frac{\widetilde{Q}}{\widetilde{W}}\right)^2 + \frac{2}{\alpha}\frac{\widetilde{Q}}{\widetilde{W}^2}}\right)\right] \tag{A.5}$$

with $\widetilde{l}_{slip} = l_{slip}/a$.

Equations (A.4,A.5) hold when all the punch is in contact with the half-plane. If the tangential load is further increased $\widetilde{Q} = \alpha$ lift-off happens at $x = -a$ and a partial contact condition is obtained. In the latter case the normal load is no longer center positioned with respect to the actual contact area of width $2a\prime$ thus the equivalent momentum is $Qh - P(a-a')$. Replacing Qh with $Qh - P(a-a')$ in (3.2) the pressure distribution is

$$\widetilde{p}(x') = \frac{\alpha}{f\left(2\alpha - \widetilde{Q}\right)}\sqrt{\frac{a'+x'}{a'-x'}} \tag{A.6}$$

with

$$a' = a\left(2 - \frac{Q}{\alpha P f}\right); \qquad x' = x - (a - a') \tag{A.7}$$

and $\widetilde{p}(x') = \frac{p(x')}{fP/(\pi a)}$. When $a' = 0$ the tip over occurs so

$$Q_{to} = 2fP\alpha \tag{A.8}$$

In the range $-a' < x' < -b'$ the shear tractions are proportional to the pressure via the coefficient of friction f

$$\widetilde{q}(x') = \frac{\alpha}{2\alpha - \widetilde{Q}}\sqrt{\frac{a' + x'}{a' - x'}} \tag{A.9}$$

In the stick zone $-b' < x' < a'$ the dimensional shear tractions are

$$\int_{-b'}^{a'} \frac{q^*\left(\xi\right)d\xi}{x' - \xi} = -\int_{-a'}^{a'} \frac{fp\left(\xi\right)d\xi}{x' - \xi} = \frac{2f[Qh - P(a - a')]}{a'^2} \tag{A.10}$$

If we define

$$h^* = h - \frac{P}{Q}(a - a') \tag{A.11}$$

equation (A.10) becomes

$$\int_{-b'}^{a'} \frac{q^*\left(\xi\right)d\xi}{x' - \xi} = \frac{2fQh^*}{a'^2} = \frac{Q}{\alpha^* a'} \tag{A.12}$$

which is identical to eq. (**??**) but with $\alpha^* = \frac{a'}{2fh^*} = \widetilde{Q}$. Following the same argumentation presented before, the solution of eq. (A.12) is

$$q^*(x') = -\frac{fP}{\pi a'}\sqrt{\frac{b' + x'}{a' - x'}} + K_{II}\sqrt{\frac{a' + b'}{2\pi\left(x' + b'\right)\left(a' - x'\right)}} \tag{A.13}$$

thus the shear traction within the stick zone will be $(-b' < x' < a')$

$$q(x') = fp(x') + q^*(x') = \tag{A.14}$$

$$= \frac{fP}{\pi a'}\left(\sqrt{\frac{a' + x'}{a' - x'}} - \sqrt{\frac{b' + x'}{a' - x'}}\right) + \sqrt{\frac{E^*W}{\pi}}\sqrt{\frac{\left(a' + b'\right)}{\left(x' + b'\right)\left(a' - x'\right)}} \tag{A.15}$$

that for $K_{II} = 0$ (i.e. $W = 0$) coincides with the adhesiveless solution already found in [36]. After some algebra the dimensionless length of the slip front is

$$\widetilde{l}_{slip} = \frac{\widetilde{Q}}{\alpha} - \left(2 - \frac{\widetilde{Q}}{\alpha}\right)\left(1 + 4\widetilde{W}^2 + \frac{2}{\alpha}\left[\widetilde{W}\sqrt{\left(2\alpha - \widetilde{Q}\right)\left[2\alpha\left(\widetilde{W}^2 + 1\right) - \widetilde{Q}\left(2\alpha + \widetilde{W}^2\right)\right]} - \widetilde{Q}\left(\alpha + W^2\right)\right]\right) \tag{A.16}$$

Appendix B

Consider the most general case in which the normal load has a general phase δ with respect to the tangential load. For positive velocity, we have from equilibrium,

$$v(t) = \frac{Q_1}{k}\sin(\omega_d t) - \frac{f}{k}\left[N_0 + N_1 \sin(\omega_d t + \delta)\right] \tag{B.1}$$

The temporal evolution of the displacement depends on

$$\frac{Q_1}{k}\sin(\omega_d t) - \frac{f}{k}N_1 \sin(\omega_d t + \delta) \tag{B.2}$$

Notice that if we turn to the phasor representation, the (B.2) is the projection on the y-axis of the two rotating vectors of magnitude $\frac{Q_1}{k}$ and $\frac{fN_1}{k}$, those rotate counterclockwise at the angular velocity ω_d. Our scope is to reduce those to a single equivalent vector $\bar{R}$ of magnitude $\left\lVert \bar{R} \right\rVert$ that rotates at the same angular velocity but with an arbitrary phase α. Looking to the Fig. 9 on the left and making use of some geometric laws we obtain:

$$\left\lVert \bar{R}_{fs} \right\rVert = \sqrt{\left(\frac{Q_1}{k}\cos(\delta) - \frac{f}{k}N_1\right)^2 + \left(\frac{Q_1}{k}\sin(\delta)\right)^2} =$$
$$= \frac{Q_1}{k}\sqrt{1 + \beta^2\eta^2 - 2\beta\eta\cos(\delta)} \tag{B.3}$$

and phase

$$\alpha_{fs} = \begin{cases} \arcsin\left(\frac{\sin(\delta)}{\sqrt{1+\beta^2\eta^2-2\beta\eta\cos(\delta)}}\right) - \delta & \text{for } \cos(\delta) \geq \beta\eta \\[4mm] \pi - \delta - \arcsin\left(\frac{\sin(\delta)}{\sqrt{1+\beta^2\eta^2-2\beta\eta\cos(\delta)}}\right) & \text{for } \cos(\delta) < \beta\eta \end{cases} \tag{B.4}$$

The terms (B.2) during the forward slip phase can be replaced by $\left\lVert \bar{R}_{fs} \right\rVert \sin(\omega_d t - \alpha_{fs})$ using (B.3) and (B.4) and thus the displacements and velocities are equal to

$$\widetilde{v}_{fs}(t) = -\beta + \sqrt{1 + \beta^2\eta^2 - 2\beta\eta\cos(\delta)}\sin(\omega_d t - \alpha_{fs}) =$$
$$= -\beta + \sqrt{1 + \beta^2\eta^2 - 2\beta\eta\cos(\delta)}g_2^\delta(t) \tag{B.5}$$

$$\dot{\widetilde{v}}_{fs}(t) = \sqrt{1 + \beta^2\eta^2 - 2\beta\eta\cos(\delta)}\cos(\omega_d t - \alpha_{fs}) =$$
$$= \frac{1}{\omega_d}\sqrt{1 + \beta^2\eta^2 - 2\beta\eta\cos(\delta)}\dot{g}_2^\delta(t) \tag{B.6}$$

where we introduced the function $g_2^\delta(t) = \sin(\omega_d t - \alpha_{fs})$, as the analogue of the function $g(t)$ introduced previously. Looking to the Fig. A.1, on the right side we can see the rotating vectors plane for the case of backward slip. The equivalent rotating vector has magnitude $\left\lVert \bar{R}_{bs} \right\rVert$

$$\left\| \bar{R}_{bs} \right\| = \sqrt{\left(\frac{Q_1}{k} \cos(\delta) + \frac{f}{k} N_1 \right)^2 + \left(\frac{Q_1}{k} \sin(\delta) \right)^2} =$$
$$= \frac{Q_1}{k} \sqrt{1 + \beta^2 \eta^2 + 2\beta\eta \cos(\delta)} \tag{B.7}$$

and phase

$$\alpha_{bs} = \begin{cases} \delta - \arcsin \left(\frac{\sin(\delta)}{\sqrt{1 + \beta^2 \eta^2 + 2\beta\eta \cos(\delta)}} \right) & \text{for } \cos(\delta) \geq -\beta\eta \\[3mm] -\pi + \delta + \arcsin \left(\frac{\sin(\delta)}{\sqrt{1 + \beta^2 \eta^2 - 2\beta\eta \cos(\delta)}} \right) & \text{for } \cos(\delta) < -\beta\eta \end{cases} \tag{B.8}$$

Hence, we can express displacements and velocities as

$$\widetilde{v}_{bs}(t) = \beta + \sqrt{1 + \beta^2 \eta^2 + 2\beta\eta \cos(\delta)} \sin(\omega_d t + \alpha_{bs}) =$$
$$= \beta + \sqrt{1 + \beta^2 \eta^2 + 2\beta\eta \cos(\delta)} g_1^\delta(t) \tag{B.9}$$

$$\dot{\widetilde{v}}_{bs}(t) = \sqrt{1 + \beta^2 \eta^2 + 2\beta\eta \cos(\delta)} \cos(\omega_d t + \alpha_{bs}) =$$
$$= \frac{1}{\omega_d} \sqrt{1 + \beta^2 \eta^2 + 2\beta\eta \cos(\delta)} \dot{g}_1^\delta(t) \tag{B.10}$$

where we have introduced the function $g_1^\delta(t) = \sin(\omega_d t + \alpha_{bs})$.
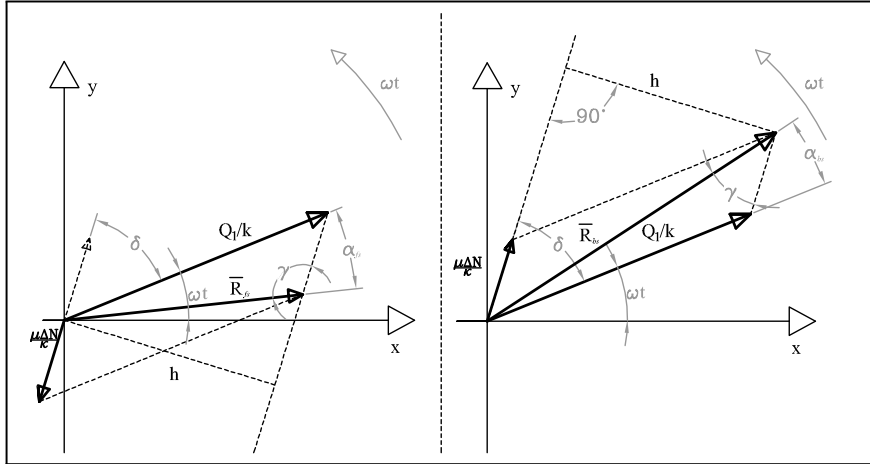
Figure A.1 Displacements as rotating vectors. On the left for forward slip, on the right for backward slip.

Looking to (B.1),(B.9),(B.3) we can derive that the maximum displacement will be reached when $g_2^\delta(t)$ will reach its highest value (=1), while the minimum displacement will correspond to $g_1^\delta(t) = -1$, obtaining

$$\widetilde{v}_{\max}^\delta = -\beta + \sqrt{1 + \beta^2 \eta^2 - 2\beta\eta \cos(\delta)} \tag{B.11}$$

$$\widetilde{v}_{\min}^\delta = \beta - \sqrt{1 + \beta^2 \eta^2 + 2\beta\eta \cos(\delta)} \tag{B.12}$$

From (B.11) and (B.12) for $\left(\widetilde{v}^{\delta}_{\max}\widetilde{v}^{\delta}_{\min}\right) < 0$ is straightfoward to deduce a general formula to predict the dimensionless maximum displacement in modulus

$$\left|\widetilde{v}^{\delta}_{\max}\right| = -\beta + \sqrt{1 + \beta^2\eta^2 + 2\beta\eta\left|\cos(\delta)\right|} \tag{B.13}$$

otherwise the simplest way is of course to compare $\widetilde{v}^{\delta}_{\max}$ and $\widetilde{v}^{\delta}_{\min}$. The reader will be careful in this comparison as the minimum (maximum) displacement is not necessarily negative (positive). Obviously, we can give the result in terms of amplitude as

$$\widetilde{v}^{\delta}_{a} = -\beta + \frac{1}{2}\left(\sqrt{1 + \beta^2\eta^2 - 2\beta\eta\cos(\delta)} + \sqrt{1 + \beta^2\eta^2 + 2\beta\eta\cos(\delta)}\right) \tag{B.14}$$

Switching to velocity, in the rotating vector plane, equations (B.9) and (B.10) define two rotating vectors rotating at the same angular frequency with a phase angle of 90°. When the backward slip commences, if $\left\|\bar{R}_{bs}\right\|\sin(\omega_d t + \alpha_{bs})$ is still positive, then the maximum velocity will be reached when $\frac{d\bar{R}_{bs}}{dt}$ will cross the y-axis otherwise if $\left\|\bar{R}_{bs}\right\|\sin(\omega_d t + \alpha_{bs})$ has become negative then the maximum velocity will be that exactly in the instant in which the backward slip commences. For the first case, the magnitude of the maximum velocity is exactly $\omega_d\left\|\bar{R}_{bs}\right\|$ (i.e. $\cos(\omega_d t + \alpha_{bs}) = -1$), while for the second we can equate equations (B.11) and (B.9) at the time instant t_{bs} in which the backward slip commences obtaining

$$g^{\delta}_1(t_{bs}) = \frac{-2\beta + \sqrt{(1 + \beta^2\eta^2 - 2\beta\eta\cos(\delta))}}{\sqrt{1 + \beta^2\eta^2 + 2\beta\eta\cos(\delta)}} \tag{B.15}$$

Studying the sign of the equation (B.15), we obtain that

$$g^{\delta}_1(t_{bs}) < 0 \text{ for } \beta > \beta_1 = \frac{\eta\cos(\delta) - \sqrt{4 - \eta^2 + \eta^2\cos^2(\delta)}}{\eta^2 - 4} \tag{B.16}$$

When the condition (B.16) holds we need to compute the velocity at the onset of slip (i.e. the maximum reached in the backward slip phase). For this purpose we compute $\omega_d t_{bs} + \alpha_{bs} = \pi - \arcsin(g^{\delta}_1(t_{bs}))$ and thus substituting into (B.10) after some mathematics we obtain in magnitude the maximum velocity reached during the backward slip

$$\left|\dot{\widetilde{v}}_{bs}(t_{bs})\right| = 2\sqrt{\beta\left(\eta\cos(\delta) - \beta + \sqrt{1 + \beta^2\eta^2 - 2\beta\eta\cos(\delta)}\right)} \tag{B.17}$$

The mass is moving now towards the negative direction and will reach the maximum negative displacement reported in (B.12). The mass will be stuck for a while, then will start again to move, but in the positive direction. If $\left\|\bar{R}_{fs}\right\|\sin(\omega_d t - \alpha_{fs})$ is still negative when the forward slip starts then the maximum positive velocity will be that corresponding to the maximum value of $\dot{g}^{\delta}_2(t)/\omega_d = \cos(\omega_d t - \alpha_{fs})$, i.e. 1, thus $\left|\dot{v}_{fs}(t)\right|_{\max} = \omega_d\left\|\bar{R}_{fs}\right\|$. If $g^{\delta}_2(t)$ turns to the positive sign then we need to compute the value of $g^{\delta}_2(t_{fs})$ at the time instant in which the forward slip commences. When it happens $\widetilde{v}$ is equal to $\widetilde{v}^{\delta}_{\min}$ thus equating (B.12) and (B.5) we obtain:

$$g^{\delta}_2(t_{fs}) = \frac{2\beta - \sqrt{(1 + \beta^2\eta^2 + 2\beta\eta\cos(\delta))}}{\sqrt{1 + \beta^2\eta^2 - 2\beta\eta\cos(\delta)}} \tag{B.18}$$

Studying the sign of $g^{\delta}_2(t_{fs})$ we find that

$$g^{\delta}_2(t_{fs}) > 0 \text{ for } \beta > \beta_2 = \frac{\eta\cos(\delta) + \sqrt{4 - \eta^2 + \eta^2\cos^2(\delta)}}{4 - \eta^2} \tag{B.19}$$

For this case $\omega_d t_{fs} - \alpha_{fs} = \arcsin(g_2^\delta(t_{fs}))$, and computing $\dot{v}_{fs}(t_{fs})$ we obtain

$$\dot{\tilde{v}}_{fs}(t_{fs}) = 2\sqrt{-\beta\left(\beta + \eta\cos(\delta) - \sqrt{1 + \beta^2\eta^2 + 2\beta\eta\cos(\delta)}\right)} \tag{B.20}$$

To sum up all the relations found

$$\left|\dot{\tilde{v}}_{bs}\right|_{\max} = \begin{cases} \sqrt{1 + \beta^2\eta^2 + 2\beta\eta\cos(\delta)} & \text{for } \beta \leqslant \beta_1 \\ 2\sqrt{\beta\left(\eta\cos(\delta) - \beta + \sqrt{1 + \beta^2\eta^2 - 2\beta\eta\cos(\delta)}\right)} & \text{for } \beta > \beta_1 \end{cases} \tag{B.21}$$

$$\left.\dot{\tilde{v}}_{fs}\right|_{\max} = \begin{cases} \sqrt{1 + \beta^2\eta^2 - 2\beta\eta\cos(\delta)} & \text{for } \beta \leqslant \beta_2 \\ 2\sqrt{-\beta\left(\beta + \eta\cos(\delta) - \sqrt{1 + \beta^2\eta^2 + 2\beta\eta\cos(\delta)}\right)} & \text{for } \beta > \beta_2 \end{cases} \tag{B.22}$$

The inequalities introduced in (B.21) and (B.22) divide the plane (β, η) into 3 regions (which collapse in 2 regions for $\delta = 90°$). In each region 2 of the above equations hold, one for the forward the other for the backward slip phase, thus in general given (β, η, δ) one needs to check which of the two velocity is greater in magnitude.

Starting from the above results we provide the general formula for energy dissipation for out-of-phase loading. Firstly we evaluate the energy dissipated during backward slip phase i.e. between t_{bs} and $t_{stop,bs}$

$$W_1 = \int_{t_{bs}}^{t_{stop,bs}} \dot{W} dt = \int_{t_{bs}}^{t_{stop,bs}} -F\dot{v}_{bs} dt \tag{B.23}$$

where $F = f\left(N_0 + N_1\sin(\omega_d t + \delta)\right)$. Solving the integral (B.23), we obtain

$$W_1 = \frac{Q_1^2}{k}\beta\sqrt{1 + \beta^2\eta^2 + 2\beta\eta\cos(\delta)}\left\{1 + g_1^\delta(t_{bs}) - \frac{\eta}{4}\left[\cos(2\omega_d t_{bs} + \alpha_{bs} + \delta)+\right.\right.$$
$$\left.\left. - \cos(2\omega_d t_{stop,bs} + \alpha_{bs} + \delta) - 2\omega_d\left(t_{stop,bs} - t_{bs}\right)\sin(\alpha_{bs} - \delta)\right]\right\} \tag{B.24}$$

where $g_1^\delta(t_{bs})$ is computed with (B.15), while t_{bs} and $t_{stop,bs}$ are respectively

$$t_{bs} = \frac{1}{\omega_d}\left[\pi - \arcsin(g_1^\delta(t_{bs})) - \alpha_{bs}\right] \tag{B.25}$$

$$t_{stop,bs} = \frac{1}{\omega_d}\left[\frac{3}{2}\pi - \alpha_{bs}\right] \tag{B.26}$$

During the forward slip phase, the dissipated energy is

$$W_2 = \int_{t_{fs}}^{t_{stop,fs}} \dot{W} dt = \int_{t_{fs}}^{t_{stop,fs}} -F\dot{v}_{fs} dt \tag{B.27}$$

where $F = -f\left(N_0 + N_1\sin(\omega_d t + \delta)\right)$. Solving (B.27) we obtain

$$W_2 = \frac{Q_1^2}{k}\beta\sqrt{1 + \beta^2\eta^2 - 2\beta\eta\cos(\delta)}\left\{1 - g_2^\delta(t_{fs}) + \frac{\eta}{4}\left[\cos(2\omega_d t_{fs} - \alpha_{fs} + \delta)+\right.\right.$$
$$\left.\left. - \cos(2\omega_d t_{stop,fs} - \alpha_{fs} + \delta) + 2\omega_d\left(t_{stop,fs} - t_{fs}\right)\sin(\alpha_{fs} + \delta)\right]\right\} \tag{B.28}$$

where $g_2^\delta(t_{fs})$ is computed with (B.18) while t_{fs} and $t_{stop,fs}$ are respectively

$$t_{fs} = \frac{1}{\omega_d} \left[\arcsin(g_2^\delta(t_{fs})) + \alpha_{fs} \right] \tag{B.29}$$

$$t_{stop,fs} = \frac{1}{\omega_d} \left[\frac{\pi}{2} + \alpha_{fs} \right] \tag{B.30}$$

The total amount of energy dissipated in a cycle will be $W = W_1 + W_2$. For the case of quadrature loading (B.24) and (B.28) give

$$W|_{\delta=90°} = 4fN_0 \frac{Q_1}{k} \left(\frac{\sqrt{1 + \beta^2 \eta^2} - \beta}{1 + \beta^2 \eta^2} \right) \tag{B.31}$$

Acknowledgments

I wish to thank my tutor Prof. Ing. M. Ciavarella for the great help he gave me during my Ph.D. course. His meaningful suggestions and his clever understanding of the contact mechanics theory supported my work, and gave me the opportunity to grow as a researcher. I wish to thank Prof. N. Hoffmann which hosted me at Imperial College in London. Also I would like to thank my family and my girlfriend Elena for having been always by my side during these three years that will leave an invaluable sign in my life.

Antonio

Bibliography

[1] Hills, D. A., Nowell D., and Sackfield A., Mechanics of elastic contacts, 1993. Butterworth-Heinemann, Oxford.

[2] Johnson, K.L. Contact Mechanics. Cambridge University Press, 1985.

[3] Timoshenko, S. P., and Goodier J. N., Theory of elasticity. 1982. MacGraw Hill International Book.

[4] Muskhelishvili, N. I., Singular Integral Equations: Boundary Problems of Functions Theory and Their Application to Mathematical Physics, 1953. J. R. M. Radok (Ed.). P. Noordhoff.

[5] Dundurs, J., Edge-bonded dissimilar orthogonal elastic wedges under normal and shear loading, 1969. Journal of applied mechanics, 36(3), 650-652. ISO 690

[6] Cattaneo, C., Sul contatto di due corpi elastici: Distribuzion locale degli sforzi. Reconditi dell Accademia nazionale dei Lincei, 1938. 27: 342-248, 434-436, 474-478.

[7] Mindlin, R. D., Compliance of Elastic Bodies in Contact. J. of Appl. Mech. 1949; 16.

[8] Ciavarella, M., The generalized Cattaneo partial slip plane contact problem I-Theory. Int. J. Solids Struct. 1998a; 35/18: 2349-2362.

[9] Ciavarella, M. The generalized Cattaneo partial slip plane contact problem. II—Examples. International journal of solids and Structures, 1998, 35(18), 2363-2378.

[10] Ciavarella, M.,Tangential loading of general three-dimensional contacts. ASME J. Appl. Mech. 1998b; 65: 998–1003.

[11] Persson, B. N. J., Sliding Friction: Theory and Applications, 1998.

[12] Bowden F.P., Tabor D., The Friction and Lubrication of Solids, Clarendon Press, Oxford, 1950.

[13] Greenwood, J.A. and Williamson, J.B.P., Contact of Nominally Flat Surfaces, Proc. R. Soc. Lond. A, 1966, vol. 295 no. 1442 300-319.

[14] Rabinowicz, E., Friction and wear of materials. John Wiley & Sons, New York, 1965.

[15] Rice, J.R., Heating and weakening of faults during earthquake slip. J. Geophys.Res., 2006, 111, B05311, doi:10.1029/2005JB004006.

[16] Dieterich, J.H., Modeling of rock friction 1. Experimental results and constitutive equations. J. Geophys. Res., 1979, 84, 2161-2168.

[17] Ruina, A.L., Slip instability and state variable friction laws. J. Geophys. Res. 1983, 88,10359-10370.

[18] Dieterich, J.H., Applications of Rate- and State-Dependent Friction to Models of Fault Slip and Earthquake Occurrence, Treatise on Geophysics, 2007, Chapter 4.04, Pages 107-129.

[19] Rubinstein, S. M., Cohen, G., and Fineberg, J., Detachment fronts and the onset of dynamic friction. Nature 2004; 430: 1005-1009.

[20] Rubinstein, S. M., Cohen, G., & Fineberg, J. Dynamics of precursors to frictional sliding. Phys Rev Letters 2007; 98(22), 226103.

[21] Rubinstein, S. M., G. Cohen, and J. Fineberg. Visualizing stick–slip: experimental observations of processes governing the nucleation of frictional sliding. Journal of Physics D: Applied Physics, 2009, 42.21: 214016.

[22] Ben-David, O., Cohen G and Fineberg, J. The Dynamics of the Onset of Frictional Slip. Science 2010a; 330 no. 6001: 211-214

[23] Ben-David O, Rubinstein SM., & Fineberg J. Slip-stick and the evolution of frictional strength. Nature 2010; 463.7277: 76-79.

[24] Ben-David, O., and Fineberg, J. Static Friction Coefficient Is Not a Material Constant. Phys. Rev. Lett. 2011; 106: 254301.

[25] Svetlizky, I., and Fineberg, J., Classical shear cracks drive the onset of dry frictional motion. Nature 2014; 509: 205–208.

[26] Scheibert, J., and Dysthe, D. K., Role of friction-induced torque in stick-slip motion. EPL (Europhysics Letters), 2010, 92(5), 54001.

[27] Papangelo, A., Stingl, B., Hoffmann, N.P., and Ciavarella, M., A simple model for friction detachment at an interface of finite size mimicking Fineberg's experiments on uneven loading, Phys.Mesomech., 2014, 17, 311.

[28] Bouchbinder, E., Brener, E. A., Barel, I., & Urbakh, M. Slow cracklike dynamics at the onset of frictional sliding. Physical review letters, 2011, 107(23), 235501.

[29] Bar Sinai, Y., Brener, E. A., and Bouchbinder, E., Slow rupture of frictional interfaces. Geophysical Research Letters, 2012, 39.3.

[30] Trømborg, J., Scheibert, J., Amundsen, D. S., Thøgersen, K., & Malthe-Sørenssen, A., Transition from static to kinetic friction: insights from a 2D model. Physical review letters, 2011, 107(7), 074301.

[31] Trømborg, J. K., Sveinsson, H. A., Scheibert, J., Thøgersen, K., Amundsen, D. S., & Malthe-Sørenssen, A., Slow slip is a mechanism for slow fronts in the rupture of frictional interfaces. arXiv preprint, 2014, arXiv:1402.4700.

[32] Kammer, D. S., Yastrebov, V. A., Spijker, P., & Molinari, J. F., On the propagation of slip fronts at frictional interfaces. Tribology Letters, 2012, 48(1), 27-32.

[33] Kammer, D. S., Radiguet, M., Ampuero, J. P., & Molinari, J. F., Linear elastic fracture mechanics predicts the propagation distance of frictional slip. Tribology Letters, 2015, 57(3), 1-10.

[34] Romero, V., Wandersman, E., Debregeas, G., and Prevost, A., Probing locally the onset of slippage at a model multicontact interface. Physical review letters 2014, 112(9), 094301.

[35] Taloni, A., Benassi, A., Sandfeld, S., & Zapperi, S. Scalar model for frictional precursors dynamics. Scientific reports 2015; 5.

[36] Grimaldi, G., A. Papangelo, and M. Ciavarella. A Cattaneo-Mindlin problem for a rigid punch with tangential load applied above the interface line. Proceedings of the Institution of Mechanical Engineers, Part C 230.9 2016: 1410-1416.

[37] Papangelo, A., and Ciavarella, M., Cattaneo–Mindlin plane problem with Griffith friction. Wear 342, 2015: 398-407.

[38] Papangelo, A., Ciavarella, M., Barber, J.R., Fracture Mechanics implications for apparent static friction coefficient in contact problems involving slip-weakening laws. submitted to Proc Roy Soc-A, 2015.

[39] Barber, J. R., Elasticity. Dordrecht: Kluwer academic publishers, 2002.

[40] Sackfield, A., Truman, C. E., and Hills, D. A. The tilted punch under normal and shear load (with application to fretting tests). International Journal of mechanical sciences 2001; 43(8), 1881-1892.

[41] Johnson, K.L., Energy dissipation at spherical surfaces in contact transmitting oscillating forces, J. Mech. Eng. Sci., 1961, 3, 362–368.

[42] Popp, K., Panning, L., Sextro, W., Vibration damping by friction forces: theory and applications. J Vib Control, 2003, 9, 419–448.

[43] Nowell D, Dini D, Hills DA. Recent developments in the understanding of fretting fatigue. Eng Fract Mech. 2006, 73, 207–222.

[44] Popp, K., Stelter, P., Stick-slip vibrations and chaos.Phil. Trans. R. Soc. Lond., 1990, 332, 89–105.

[45] Rabinowicz, E., The nature of the static and kinetic coefficients of friction. Journal of applied physics, 1951, 22(11), 1373-1379.

[46] Feynman, R. P. , Leighton, R. P. and Sands M., The Feynman Lectures on Physics, 1964, Vol. I, p. 12-2, Addison-Wesley.

[47] Poliakov, A. N. B., Dmowska, R.& Rice, J. R., Dynamic shear rupture interactions with fault bends and off-axis secondary faulting. J. Geophys. Res., 2002, 107(B11), 2295.

[48] Rice, J. R. Low-stress faulting: Strong but brittle faults with local stress concentrations, Eos Trans. AGU, 1996, 77(46), Fall Meet. Suppl., F471

[49] Rice, J.R., Lapusta, N., Ranjith, K., Rate and state dependent friction and the stability of sliding between elastically deformable solids. J. Mech. Phys. Solids, 2001, 49, 1865–1898.

[50] Munisamy, R.L., Hills, D.A., Nowell, D., Static axisymmetrical Hertzian contacts subject to shearing forces. ASME J.Appl. Mech., 1994, 61, 278–283

[51] Abercrombie R.E., Rice J.R., Can observations of earthquake scaling constrain slip weakening? Geophys.J. Int., 2005, 162, 406–424.

[52] Jager, J., A new principle in contact mechanics. Journal of tribology, 1998, 120(4), 677-684.

[53] Ben-Zion, Y., Collective behavior of earthquakes and faults: Continuum-discrete transitions, progressive evolutionary changes, and different dynamic regimes. Reviews of Geophysics, 2008, 46(4).

[54] Maugis, D., Adhesion of spheres: The JKR-DMT transition using a Dugdale model. J. Colloid Interface Sci., 1992, 150, 243–269.

[55] Greenwood, J.A., Johnson, K.L., An alternative to the Maugis model of adhesion between elastic spheres. J. Phys. D: Applied Physics., 1998, 31, 3279–3290.

[56] Ciavarella, M., Transition from stick to slip in Hertzian contact with "Griffith" friction: the Cattaneo-Mindlin problem revisited. Journal of the Mechanics and Physics of Solids, 2015, 84, 313–324.

[57] Rice, J.R., Limitations to the small scale yielding approximation for crack tip plasticity, Journal of the Mechanics and Physics of Solids, 1974, Vol. 22, 17–26.

[58] ANSYS Mechanical APDL Verification Manual - VM272: 2-D and 3-D Frictional Hertz Contact, ANSYS, Inc. Release 15.0 November 2013, 785–788

[59] Yang, B., Laursen, T.A., Meng, X., Two dimensional mortar contact methods for large deformation frictional sliding.Int. J. Numer. Meth. Engng., 2005, 62 1183–1225. doi: 10.1002/nme.1222

[60] Ida, Y., Cohesive force across tip of a longitudinal-shear crack and Griffiths specific surface energy. J. Geophys. Res., 1972, 77, 3796–3805

[61] Palmer, A.C., and Rice, J.R., The growth of slip surfaces in the progressive failure of over-consolidated clay. Proc. R. Soc. Lond. A, 1973, 332, 527–548

[62] Scholz, C. H. The Mechanics of Earthquakes and Faulting 2nd edn, 2002, Cambridge Univ. Press, Cambridge.

[63] Brener, E. A., and Marchenko, V. I., Frictional shear cracks. Journal of Experimental and Theoretical Physics Letters, 2002, 76(4), 211-214.

[64] Persson, B. N.; Volokitin, A. I., Theory of rubber friction: Nonstationary sliding. Physical Review B, 2002, 65 (13): 134106

[65] Popov, V.L., Hess, M., Method of Dimensionality Reduction in Contact Mechanics and Friction, 2015, Springer-Verlag Berlin.

[66] Johnson, K. L., Kendall, K. & Roberts, A. D., Surface Energy and the Contact of Elastic Solids. Proc. R. Soc. London Ser. A, 1971, 324, 301–320.

[67] Johnson, K. L. The adhesion of two elastic bodies with slightly wavy surfaces. International Journal of Solids and Structures, 1995, 32(3), 423-430.

[68] Westergaard, H. M., Bearing Pressures and Cracks. Journal of applied mechanics, 1939, A49-A53

[69] Prevost, A., Scheibert, J., & Debrégeas, G., Probing the micromechanics of a multi-contact interface at the onset of frictional sliding. The European Physical Journal E 2013; 36(2), 1-12.

[70] Persson, B. N., Albohr, O., Mancosu, F., Peveri, V., Samoilov, V. N., & Sivebæk, I. M., On the nature of the static friction, kinetic friction and creep. Wear, 2003, 254(9), 835-851.

[71] Hanson, R.D., Wu, J.P., and Ashour, S.A., Effect of Large Damping on Earthquake Response, Proceedings of the 9th World Conference on Earthquake Engineering. 1988.

[72] Gandhi, F., and Chapuis, Passive damping augmentation of a vibrating beam using pseudoelastic shape memory alloy wires. Journal of Sound and vibration 2002; 250.3: 519-539.

[73] Ashour S.A., Elastic seismic response of building with supplemental damping, PhD Thesis, Michigan University, Ann Arbor, USA, 1987.

[74] Hanson, R. D., Aiken, I. D., Nims, D. K., Richter, P. J., & Bachman, R. E., State-of-the-art and state-of-the-practice in seismic energy dissipation, Proceedings of the Seminar on Seismic Isolation, Passive Energy Dissipation, and Active Control, ATC-17-1 Rep. No. 449. Vol. 471. 1993.

[75] Hrovat, D., Barak, P., and Rabins, M., Semi-active versus passive or active tuned mass dampers for structural control. Journal of Engineering Mechanics 1983; 109.3: 691-705.

[76] Symans, M.D., and Constantinou, M.C., Semi-active control systems for seismic protection of structures: a state-of-the-art review. Engineering structures 1999; 21.6: 469-487.

[77] Aiken, I.D., Kelly, J.M., and Pall, A.S., Seismic response of a nine-story steel frame with friction damped cross-bracing. Rep. No. UCB/EERC 1988; 88: 17.

[78] Mualla, I.H., and Belev, B., Performance of steel frames with a new friction damper device under earthquake excitation. Engineering Structures 2002; 24.3: 365-371.

[79] Padmanahban, K., Murty, A., Damping in structural joints subjected to tangential loads. Proc. Inst. Mech. Eng., 1991, 205, 121–129.

[80] Padmanahban, K., Prediction of damping in machined joints. Int. J. Mach. Tools Manuf., 1992, 32, 305–31.

[81] Sanliturk, K.Y., Ewins, D.J., Stanbridge, A.B.: Underplatform dampers for turbine blades: theoretical modelling, analysis and comparison with experimental data. Journal of Engineering for Gas Turbines and Power, 2001, 123(4), 919–929.

[82] Segalman, D. J., A four-parameter Iwan model for lap-type joints. Journal of Applied Mechanics, 2005, 72(5), 752-760.

[83] Abrate, S., Modeling of impacts on composite structures. Composite Structures, 2001, 51.2, 129–138. doi: 10.1016/S0263-8223(00)00138-0

[84] Behrendt, J., Weiss, C., Hoffmann, N.P., A numerical study on stick–slip motion of a brake pad in steady sliding. Journal of Sound and Vibration, 2011, 330.4, 636–651. doi: 10.1016/j.jsv.2010.08.030

[85] Renardy, M., Ill-posedness at the boundary for elastic solids sliding under Coulomb friction. Journal of Elasticity, 1992, 27.3 281-287. doi: 10.1007/BF00041691

[86] Adams, G.G., Self-excited oscillations of two elastic half-spaces sliding with a constant coefficient of friction. Journal of Applied Mechanics, 1995, 62.4, 867-872. doi:10.1115/1.2896013

[87] Simões, F.M.F., Martins, J.A.C., Instability and ill-posedness in some friction problems. International Journal of Engineering Science, 1998, 36.11, 1265-1293. doi:10.1016/S0020-7225(98)00024-X

[88] Cochard, A., Rice, J.R., Fault rupture between dissimilar materials: Ill-posedness, regularization, and slip-pulse response. Journal of Geophysical Research, 2000, 105, 25891-25907. doi: 10.1029/2000JB900230

[89] Ranjith, K., Rice, J.R., Slip dynamics at an interface between dissimilar materials. Journal of the Mechanics and Physics of Solids, 2001, 49.2, 341-361. doi:10.1016/S0022-5096(00)00029-6

[90] Den Hartog, J.P., Forced vibrations with combined Coulomb and viscous friction. Transactions of the American Society of Mechanical Engineers, 1931, 53, pp. 107-115.

[91] Hong, H.-K., and Liu, C.–S., Non-Sticking oscillation formulae for Coulomb friction under harmonic loading. Journal of Sound and Vibration, 2001, 244.5, pp. 883–898. doi: 10.1006/jsvi.2001.3519

[92] Brake, M.R., and Hills, D.A., Determination of the limits of quasi-static/rigid and dynamic solutions for problems with frictional interfaces. Tribology International, 2014, 76: 45–56. doi: 10.1016/j.triboint .2013.09.008

[93] Hong, H.-K., and Liu, C.–S., Coulomb friction oscillator: modelling and responses to harmonic loads and base excitations. Journal of Sound and Vibration, 2000, 229.5, pp. 1171–1192. doi: 10.1006 /jsvi.1999.2594

[94] Jang, Y.H., Barber, J.R., Effect of phase on the frictional dissipation in systems subjected to harmonically varying loads. European Journal of Mechanics - A/Solids, 2011, 30.3 pp. 269–274. doi:10.1016/j.euromechsol.2011.01.008

[95] Klarbring, A., Contact problems with friction, PhD thesis, Linkoping University, Sweden, 1984.

[96] Klarbring, A., Examples of non-uniqueness and non-existence of solutions to quasi-static contact problems with friction. Ingenieur-Archiv., 1990, 60.8: 529-541.

[97] Jang, Y.H., Barber, J.R., Frictional energy dissipation in materials containing cracks. Journal of the Mechanics and Physics of Solids, 2011, 59.3, pp. 583–594. doi: 10.1016/j.jmps.2010.12.010

[98] Klarbring, A., Ciavarella, M., Barber, J.R., Shakedown in elastic contact problems with Coulomb friction. International Journal of Solids and Structures, 2007, 44.25, pp. 8355–8365. doi: 10.1016/j.ijsolstr.2007.06.013

[99] Griffin, J.H., Menq, C-H., Friction damping of circular motion and its implications to vibration control. Journal of Vibration and Acoustics, 1991, 113.2: 225-229. doi:10.1115/1.2930173

[100] Menq, C-H., Chidamparam, P., Griffin, J. H., Friction damping of two-dimensional motion and its application in vibration control. Journal of sound and vibration, 1991, 144.3: 427-447. doi:10.1016/0022-460X(91)90562-X

[101] Nims, D.K., Richter, P.J., and Bachman, R.E., The use of the energy dissipating restraint for seismic hazard mitigation. Earthquake Spectra, 1993, 9.3: 467-489.

[102] Zhou, X., and Peng, L., A new type of damper with friction-variable characteristics. Earthquake Engineering and Engineering Vibration, 2009, 8.4: 507-520.

[103] Holland, C.J., Wedge mechanism for friction shock absorbing devices. U.S. Patent No. 1975720 A, 1934.

[104] Tao, S.M., Yong, X., Baolei, W., and Guangyi, X., Oblique wedge vibration damper for railway freight car bogie, U.S. Patent No. 20130056919 A1, 2013.

[105] Shenaurin A.A. et al., Friction shock absorber for railway car truck, Russian Patent 2523513, 2014.

[106] Sanliturk, .K.Y, Ewins, D.J., Stanbridge, A.B., Underplatform dampers for turbine blades: theoretical modelling, analysis and comparison with experimental data, ASME, 1999, International Gas Turbine and Aeroengine Congress and Exhibition. ASME.

[107] Firrone, C.M., and Zucca, S., Underplatform dampers for turbine blades: The effect of damper static balance on the blade dynamics. Mechanics Research Communications 2009, 36.4: 515-522.

[108] Griffin, J.H., Friction damping of resonant stresses in gas turbine engine airfoils. Journal of Engineering for Gas Turbines and Power 1980; 102.2: 329-333.

[109] Panning, L., Sextro, W., and Popp, K., Spatial dynamics of tuned and mistuned bladed disks with cylindrical and wedge-shaped friction dampers. International Journal of Rotating Machinery 2003; 9.3: 219-228.

[110] Newmark, N.M., A Method of Computation for Structural Dynamics. Journal of the Engineering Mechanics Division, 1959; 85.3: 67-94

[111] Yang B.D., Chu M.L., and Menq C.H., Stick–slip–separation analysis and non-linear stiffness and damping characterization of friction contacts having variable normal load. Journal of Sound and vibration, 1998; 210.4: 461-481.

[112] Bazan, E, Bielak, J., and Griffin, J.H., An efficient method for predicting the vibratory response of linear structures with friction interfaces. Journal of engineering for gas turbines and power, 1986; 108.4: 633-640.

[113] Papangelo, A., and Ciavarella, M., Effect of normal load variation on the frictional behavior of a simple Coulomb frictional oscillator. Journal of Sound and Vibration, 2015; 348: 282-293

[114] Nayfeh, A.H., and Mook, D.T., Nonlinear oscillations. John Wiley & Sons, 2008.

[115] Papangelo, A., and Ciavarella, M., On the limits of quasi-static analysis for a simple Coulomb frictional oscillator in response to harmonic loads. Journal of Sound and Vibration, 2015; 339: 280-289.

[116] Champneys, A.R., Homoclinic orbits in reversible systems and their applications in mechanics, fluids and optics. Physica D: Nonlinear Phenomena, 1998, 112.1, :158-186.

[117] Umbanhowar, P.B., Melo, F., and Swinney, H.L., Localized excitations in a vertically vibrated granular layer. Nature, 1996, 382(6594), 793-796.

[118] Champneys, A.R., and Thompson, J.M.T., A multiplicity of localized buckling modes for twisted rod equations. Proceedings of the Royal Society of London A: Mathematical, Physical and Engineering Sciences, 1996, 452. No. 1954.

[119] Thompson, J.M.T., and Champneys, A.R., From helix to localized writhing in the torsional post-buckling of elastic rods. Proceedings of the Royal Society of London A: Mathematical, Physical and Engineering Sciences, 1996, Vol. 452. No. 1944. The Royal Society.

[120] Lord, G.J., Champneys, A.R., and Hunt, G.W., Computation of localized post buckling in long axially compressed cylindrical shells. Philosophical Transactions of the Royal Society of London A: Mathematical, Physical and Engineering Sciences, 1997, 355.1732: 2137-2150.

[121] Hunt, G.W., Peletier, M.A., Champneys, A.R., Woods, P.D., Wadee, M.A., Budd, C.J., and Lord, G.J., Cellular buckling in long structures. Nonlinear Dynamics, 2000, 21.1 : 3-29.

[122] Grolet, A., and Thouverez, F., Vibration analysis of a nonlinear system with cyclic symmetry. Journal of Engineering for Gas Turbines and Power, 2011, 133(2), 022502.

[123] Grolet, A. and Thouverez, F., Free and forced vibration analysis of a nonlinear system with cyclic symmetry: Application to a simplified model. Journal of sound and vibration, 2012, 331(12), 2911-2928.

[124] Niemela, J.J., Ahlers, G., and Cannell, D.S., Localized traveling-wave states in binary-fluid convection. Physical review letters, 1990, 64.12: 1365.

[125] Woodcraft, A.L., Lucas, P.G.J., Matley, R.G., and Wong, W.Y.T., Visualisation of convective flow patterns in liquid helium. Journal of low temperature physics, 1999, 114(1-2), 109-134.

[126] Batiste, O., Knobloch, E., Alonso, A., and Mercader, I., Spatially localized binary-fluid convection. Journal of Fluid Mechanics, 2006, 560, 149-158.

[127] Beaume, C., Bergeon, A., and Knobloch, E., Homoclinic snaking of localized states in doubly diffusive convection. Physics of Fluids, 2011, 23(9), 094102.

[128] Thual, O., and Fauve, S., Localized structures generated by subcritical instabilities. Journal de Physique, 1988, 49.11: 1829-1833.

[129] Blanchflower, S., Magnetohydrodynamic convectons. Physics Letters A, 1999, 261.1: 74-81.

[130] Dawes, J.H.P., Localized convection cells in the presence of a vertical magnetic field. Journal of Fluid Mechanics, 2007, 570: 385-406.

[131] Burke, J., and Knobloch, E., Homoclinic snaking: structure and stability. Chaos: An Interdisciplinary Journal of Nonlinear Science, 2007, 17.3: 037102.

[132] Avitabile, D., Lloyd, D.J., Burke, J., Knobloch, E., and Sandstede, B., To snake or not to snake in the planar Swift-Hohenberg equation. SIAM Journal on Applied Dynamical Systems, 2010, 9(3), 704-733.

[133] Whitehead, D.S., Effect of mistuning on the vibration of turbo-machine blades induced by wakes. Journal of Mechanical Engineering Science, 1966, 8.1: 15-21.

[134] Ewins, D.J., The effects of detuning upon the forced vibrations of bladed disks. Journal of Sound and Vibration, 1969, 9.1: 65-79.

[135] Liu, J.K., and Zhao, L.C., Bifurcation analysis of airfoils in incompressible flow. Journal of Sound and Vibration, 1992, 154(1), 117-124.

[136] Lee, B.H.K., Price, S.J., and Wong, Y.S., Nonlinear aeroelastic analysis of airfoils: bifurcation and chaos. Progress in aerospace sciences, 1999, 35.3: 205-334.

[137] Chen, Y.M., and Liu, J.K., Supercritical as well as subcritical Hopf bifurcation in nonlinear flutter systems. Applied Mathematics and Mechanics, 2008, 29, 199-206.

[138] Pereira, D.A., Vasconcellos, R.M., Hajj, M.R., and Marques, F.D., Insights on aeroelastic bifurcation phenomena in airfoils with structural nonlinearities. Mathematics in Engineering, Science & Aerospace (MESA), 2015, 6(3).

[139] Weiss, C., Morlock, M.M., and Hoffmann, N., Friction induced dynamics of ball joints: Instability and post bifurcation behavior. European Journal of Mechanics-A/Solids, 2014, 45, 161-173.

[140] Gräbner, N., Tiedemann, M., Von Wagner, U., and Hoffmann, N., Nonlinearities in Friction Brake NVH-Experimental and Numerical Studies (No. 2014-01-2511). SAE Technical Paper.

[141] Yulin, A.V., and Champneys, A.R., Discrete snaking: multiple cavity solitons in saturable media. SIAM Journal on Applied Dynamical Systems, 2010 ,9(2), 391-431.

[142] Taylor, C., and Dawes, J.H., Snaking and isolas of localised states in bistable discrete lattices. Physics Letters A, 2010, 375(1), 14-22.

[143] Billah, K.Y., and Scanlan, R.H., Resonance, Tacoma Narrows bridge failure, and undergraduate physics textbooks. American Journal of Physics, 1991, 59(2), 118-124.

[144] Rudd, M.J., Wheel/rail noise—part II: wheel squeal. Journal of Sound and Vibration, 1976, 46(3): 381-394.

[145] Nayfeh, A.H., and Balachandran, B., Applied nonlinear dynamics: analytical, computational and experimental methods. John Wiley & Sons, 2008.

[146] Samaranayake, S., and Bajaj, A.K., Subharmonic oscillations in harmonically excited mechanical systems with cyclic symmetry. Journal of Sound and Vibration, 1997, 206(1): 39-60.

[147] Hoffmann, N., Transient growth and stick-slip in sliding friction. Journal of applied mechanics, 2006, 73(4): 642-647.